[9] Tummala PE, Chen XL, Sundell CL, et al. Angiotensin II induces vascular cell adhesion molecule-1 expression in rat vasculature: a potential link between the renin-angiotensin system and atherosclerosis. Circulation 1999;100:1223–9.
[10] Strawn WB, Chappell MC, Dean RH, Kivlighn S, Ferrario CM. Inhibition of early atherogenesis by losartan in monkeys with diet-induced hypercholesterolemia. Circulation 2000;101:1586–93.
[11] Hayek T, Attias J, Coleman R, et al. The angiotensin-converting enzyme inhibitor, fosinopril, and the angiotensin II receptor antagonist, losartan, inhibit LDL oxidation and attenuate atherosclerosis independent of lowering blood pressure in apolipoprotein E-deficient mice. Cardiovasc Res 1999;44:579–87.
[12] Dol F, Martin G, Staels B, et al. Angiotensin AT1 receptor antagonist in apolipoprotein E-deficient mice. J Cardiovasc Pharmacol 2001;38:395–405.
[13] Takai S, Kim S, Sakonjo H, Miyazaki M. Mechanisms of angiotensin II type 1 receptor blocker for anti-atherosclerotic effect in monkeys fed a high-cholesterol diet. J Hypertens 2003;21:361–9.
[14] Paigen B, Morrow A, Holmes PA, Mitchell D, Williams RA. Quantitative assessment of atherosclerotic lesions in mice. Atherosclerosis 1987;68:231–40.
[15] Ozaki M, Kawashima S, Yamashita T, et al. Overexpression of endothelial nitric oxide synthase accelerates atherosclerotic lesion formation in apoE-deficient mice. J Clin Invest 2002;110:331–40.
[16] Bradford MM. A rapid and sensitive method for the quantification of microgram quantities of protein utilizing the principle of protein-dye binding. Anal Biochem 1972;72:248–54.
[17] Munzel T, Kurz S, Rajagopalan S, et al. Hydralazine prevents nitroglycerin tolerance by inhibiting activation of a membrane-bound NADH oxidase: a new action for an old drug. J Clin Invest 1996;98:1465–70.
[18] Miller FJ, Gutterman DD, Rios CD, Heistad DD, Davidson BL. Superoxide production in vascular smooth muscle contributes to oxidative stress and impaired relaxation in atherosclerosis. Circ Res 1998;82:1298–305.
[19] Alp NJ, Mussa S, Khoo J, et al. Tetrahydrobiopterin-dependent preservation of nitric oxide-mediated endothelial function in diabetes by targeted transgenic GTP-cyclohydrolase I overexpression. J Clin Invest 2003;112:725–35.
[20] Rajagopalan S, Meng XP, Ramasamy S, Harrison DG, Galis ZS. Reactive oxygen species produced by macrophage-derived foam cells regulate the activity of vascular matrix metalloproteinases in vitro. Implications for atherosclerotic plaque stability. J Clin Invest 1996;98:2572–9.
[21] Cai H, Harrison DG. Endothelial dysfunction in cardiovascular diseases: the role of oxidative stress. Circ Res 2000;87:840–4.
[22] Warnholtz A, Nickenig G, Schulz E, et al. Increased NADH-oxidase-mediated superoxide production in the early stages of atherosclerosis: evidence for involvement of the renin-angiotensin system. Circulation 1999;99:2027–33.
[23] Pratico D, Tangirala RK, Rader DJ, Rokach J, FitzGerald GA. Vitamin E suppresses isoprostane generation in vivo and reduces atherosclerosis in ApoE-deficient mice. Nat Med 1998;4:1189–92.
[24] Schwedhelm E, Bartling A, Lenzen H, et al. Urinary 8-*iso*-prostaglandin F2alpha as a risk marker in patients with coronary heart disease: a matched case-control study. Circulation 2004;109:843–8.
[25] Schupp M, Janke J, Clasen R, Unger T, Kintscher U. Angiotensin type 1 receptor blockers induce peroxisome proliferator-activated receptor-gamma activity. Circulation 2004;109:2054–7.
[26] Benson SC, Pershadsingh HA, Ho CI, et al. Identification of telmisartan as a unique angiotensin II receptor antagonist with selective PPAR gamma-modulating activity. Hypertension 2004;43:993–1002.
[27] Sawamura T, Kume N, Aoyama T, et al. An endothelial receptor for oxidized low-density lipoprotein. Nature 1997;386:73–7.

Ventilator-induced lung injury is reduced in transgenic mice that overexpress endothelial nitric oxide synthase

Kaori Takenaka, Yoshihiro Nishimura, Teruaki Nishiuma, Akihiro Sakashita, Tomoya Yamashita, Kazuyuki Kobayashi, Miyako Satouchi, Tatsuro Ishida, Seinosuke Kawashima and Mitsuhiro Yokoyama

Am J Physiol Lung Cell Mol Physiol 290:1078-1086, 2006. First published Jan 6, 2006;
doi:10.1152/ajplung.00239.2005

AJP - Lung Cellular and Molecular Physiology publishes original research covering the broad scope of molecular, cellular, and integrative aspects of normal and abnormal function of cells and components of the respiratory system. It is published 12 times a year (monthly) by the American Physiological Society, 9650 Rockville Pike, Bethesda MD 20814-3991. Copyright © 2005 by the American Physiological Society. ISSN: 1040-0605, ESSN: 1522-1504. Visit our website at http://www.the-aps.org/.

Am J Physiol Lung Cell Mol Physiol 290: L1078–L1086, 2006.
First published January 6, 2006; doi:10.1152/ajplung.00239.2005.

Ventilator-induced lung injury is reduced in transgenic mice that overexpress endothelial nitric oxide synthase

Kaori Takenaka, Yoshihiro Nishimura, Teruaki Nishiuma, Akihiro Sakashita, Tomoya Yamashita, Kazuyuki Kobayashi, Miyako Satouchi, Tatsuro Ishida, Seinosuke Kawashima, and Mitsuhiro Yokoyama

Division of Cardiovascular and Respiratory Medicine, Department of Internal Medicine, Kobe University Graduate School of Medicine, Chuo-ku, Kobe, Japan

Submitted 1 June 2005; accepted in final form 28 December 2005

Takenaka, Kaori, Yoshihiro Nishimura, Teruaki Nishiuma, Akihiro Sakashita, Tomoya Yamashita, Kazuyuki Kobayashi, Miyako Satouchi, Tatsuro Ishida, Seinosuke Kawashima, and Mitsuhiro Yokoyama. Ventilator-induced lung injury is reduced in transgenic mice that overexpress endothelial nitric oxide synthase. *Am J Physiol Lung Cell Mol Physiol* 290: L1078–L1086, 2006. First published January 6, 2006; doi:10.1152/ajplung.00239.2005.—Although mechanical ventilation (MV) is an important supportive strategy for patients with acute respiratory distress syndrome, MV itself can cause a type of acute lung damage termed ventilator-induced lung injury (VILI). Because nitric oxide (NO) has been reported to play roles in the pathogenesis of acute lung injury, the present study explores the effects on VILI of NO derived from chronically overexpressed endothelial nitric oxide synthase (eNOS). Anesthetized eNOS-transgenic (Tg) and wild-type (WT) C57BL/6 mice were ventilated at high or low tidal volume (V_T; 20 or 7 ml/kg, respectively) for 4 h. After MV, lung damage, including neutrophil infiltration, water leakage, and cytokine concentration in bronchoalveolar lavage fluid (BALF) and plasma, was evaluated. Some mice were given N^{ω}-nitro-L-arginine methyl ester (L-NAME), a potent NOS inhibitor, via drinking water (1 mg/ml) for 1 wk before MV. Histological analysis revealed that high V_T ventilation caused severe VILI, whereas low V_T ventilation caused minimal VILI. Under high V_T conditions, neutrophil infiltration and lung water content were significantly attenuated in eNOS-Tg mice compared with WT animals. The concentrations of macrophage inflammatory protein-2 in BALF and plasma, as well as plasma tumor necrosis factor-α and monocyte chemoattractant protein-1, also were decreased in eNOS-Tg mice. L-NAME abrogated the beneficial effect of eNOS overexpression. In conclusion, chronic eNOS overexpression may protect the lung from VILI by inhibiting the production of inflammatory chemokines and cytokines that are associated with neutrophil infiltration into the air space.

nitric oxide; acute lung injury; mechanical ventilation; macrophage inflammatory protein-2; macrophage chemoattractant protein-1

VENTILATOR-INDUCED LUNG INJURY (VILI), which is one type of acute lung injury (ALI), has the characteristics of diffuse alveolar damage, namely, an initial vascular leak with a neutrophil-predominant inflammatory response (26, 32, 33). Positive-pressure mechanical ventilation (MV) can save the lives of patients with acute respiratory distress syndrome (ARDS), and recent approaches indicate that lung protective ventilator strategies can reduce mortality during ARDS (1). A large, multicenter randomized trial has shown that MV with a lower tidal volume results in lower mortality than conventional ventilation (1). On the other hand, large tidal volumes in animal models of VILI promote cytokine release (8, 34) and cause noncardiogenic pulmonary edema with accumulation of neutrophils (3, 5).

Among the inflammatory reactions that lead to injury, nitric oxide (NO) is an important factor that regulates microvascular permeability during the pathogenesis of ALI (6, 18). NO is synthesized from L-arginine by various isoforms of NO synthase (NOS) such as constitutive neuronal NOS (nNOS, or NOS1), inducible NOS (iNOS, or NOS2), and endothelial NOS (eNOS, or NOS3). Among the three isoforms, iNOS is believed to be the only isoform that is induced by systemic or local inflammation. eNOS is usually constitutively expressed as an intracellular protein in airway epithelial and pulmonary vascular endothelial cells (4, 14). Under physiological conditions, basal NO release from endothelial cells plays important roles in the inhibition of leukocyte attachment, maintenance of mast cell stability, and reduction of platelet aggregation (18) and also protects against microvascular permeability in intestinal vessels (16). Although the pathogenesis of ALI has been explored in many animal models, the role of NO in ALI remains controversial because it has pro- as well as anti-inflammatory effects (4). We reported that chronic eNOS overexpression in the mouse endothelium results in resistance to lipopolysaccharide (LPS)-induced lung injury (35). However, because of the overwhelming amount of iNOS-related NO produced in this model, the contribution of NO from eNOS transgenic expression was difficult to interpret. The present study explores the role of overloaded eNOS in a mouse model of VILI without treatment such as LPS. We established an MV model using eNOS transgenic mice without stimulation of iNOS expression and activity. To test the hypothesis that overloaded NO suppresses VILI through neutrophil chemoattractive protein, we assessed the release of cytokines and chemokines from eNOS-overexpressing mice and performed histological evaluations.

METHODS

Animal preparation. We used 7- to 10-wk-old eNOS transgenic mice (Tg) and their wild-type (WT) littermate controls derived from the same genetic background (C57BL/6). The transgenic mice overexpress the bovine eNOS gene in the endothelium under the control of the preproendothelin-1 promoter (22). All animal experiments proceeded according to the Guidelines for Animal Experimentation at Kobe University Graduate School of Medicine.

Murine model of VILI. The mouse model of VILI was generated as described with modifications (2). Briefly, mice were anesthetized with

Address for reprint requests and other correspondence: Y. Nishimura, Division of Cardiovascular and Respiratory Medicine, Kobe Univ. Graduate School of Medicine, 7-5-1 Kusunoki-cho, Chuo-ku, Kobe 650-0017, Japan (e-mail: nishiy@med.kobe-u.ac.jp).

The costs of publication of this article were defrayed in part by the payment of page charges. The article must therefore be hereby marked "*advertisement*" in accordance with 18 U.S.C. Section 1734 solely to indicate this fact.

pentobarbital sodium (50 mg/kg ip; Abbott Laboratories, Abbott Park, IL), and the trachea was exposed under sterile conditions. A 22-gauge ventilation cannula was inserted into the trachea and sutured. The mice were placed in the supine position on a warming device and then connected to a ventilator.

We selected two types of ventilators to establish an accurate tidal volume (V_T). We used an HSE-Harvard MiniVent for the low V_T study and a Harvard Apparatus (South Natick, MA) ventilator model 683 for the high V_T study without intravascular cannulation. Blood pressure was measured using the tail-cuff method (model MK-1100; Muromachi Kikai, Tokyo, Japan) every 30 min during ventilation. The respiratory rate was adjusted to maintain pH between 7.30 and 7.45, according to arterial blood analysis. The control mice underwent tracheostomy without ventilation.

We initially examined the effect of various tidal volumes and respiratory periods. Because neutrophil recruitment into bronchoalveolar lavage fluid (BALF) was detected 4 h after ventilation, we selected this ventilation period for subsequent studies. We compared ventilation with low V_T (7 ml/kg; respiratory rate of 100 breaths/min) and high V_T (20 ml/kg; respiratory rate of 80 breaths/min). Whereas low V_T resulted in a noninvasive ventilation tidal volume, as shown elsewhere (1), high V_T used the same tidal volume that caused VILI in previous studies (6, 27). Both were maintained for 4 h at an inspiratory oxygen fraction of 0.21.

High V_T resulted in a hyperventilation state [pH: 7.414 ± 0.035; arterial P_{O_2} (Pa_{O_2}): 117.1 ± 4.4 Torr; arterial P_{CO_2} (Pa_{CO_2}): 27.0 ± 1.6 Torr; $n = 6$] compared with low V_T (pH: 7.314 ± 0.004; Pa_{O_2}: 86.8 ± 11.4 Torr; Pa_{CO_2}: 37.2 ± 5.8 Torr; $n = 6$) at the end of ventilation. Arterial blood gas data did not significantly differ between mouse groups.

The mice received 0.1 ml of 0.9% normal saline (intraperitoneally) immediately before MV started, followed by 0.1 ml of normal saline every hour thereafter. During ventilation, the mice were monitored every 30 min for adequate sedation, and pentobarbital sodium was administered as necessary. The tidal volume of the mice also was calculated by integrating airway flow during inspiration with a murine respiratory monitor (WinPULMOS II; M.I.P.S., Osaka, Japan). Some WT mice were given LPS (20 mg/kg ip; Sigma Chemical, St. Louis, MO) without MV as a positive control for iNOS induction.

To study the effects of chronic NOS inhibition on lung injury, some mice received N^{ω}-nitro-L-arginine methyl ester (L-NAME; Sigma Chemical), a potent inhibitor of NOS, in drinking water ad libitum (1 mg/ml) for 1 wk before the experiment (24).

Histopathology. Four hours after MV, the mice were killed and the lungs and trachea were removed. The right main bronchus was tightly sutured, and the whole right lung was cut to determine the wet-to-dry weight ratio (W/D ratio). The left lung was infused at a pressure of 20 cmH_2O with 10% buffered formalin, embedded in paraffin, sectioned at 5-μm thickness, and stained with hematoxylin and eosin. The histopathology of five random tissue sections from five or more lungs from each group was examined. A modified VILI histological scoring system was applied as described previously (2). Briefly, the following pathological processes were scored on a scale of 0 to 4: *1*) alveolar congestion, *2*) hemorrhage, *3*) leukocyte infiltration or aggregation of neutrophils in the air space or vessel wall, and *4*) thickness of the alveolar wall. A score of 0 represented normal lungs, and scores of 1, 2, 3, and 4 represented mild (<25%), moderate (25–50%), severe (50–75%), and very severe (>75%) lung involvement, respectively. The overall score was based on the sum of all scores. Two pathologists who were blinded to the treatment groups reviewed the degree of injury in three random sections of at least five lungs from each group of mice.

Lung water content. Lung water content related to lung injury was measured using the lung W/D ratio as described previously (27). Lung wet weight was determined immediately after removal, and the dry weight was determined after the lung was placed in an oven at 80°C for 48 h. The W/D ratio was calculated as the ratio of the wet weight to the dry weight ($n = 6$).

Bronchoalveolar lavage. After MV, the mice lungs were immediately perfused, and then BALF was obtained twice with 0.75 ml of saline ($n = 6–8$). Total cells in each sample were counted in 40-μl aliquots, using standard hematological procedures. The remaining fluid was centrifuged at 2,000 rpm for 5 min at 4°C, and cytokines were measured in the supernatants. The cell pellets were resuspended in saline, and slides were prepared by centrifugation at 400 rpm for 3 min in a Cytospin 2 (Shandon, Pittsburgh, PA). Specimens of BALF were stained.

ELISA for analysis of cytokines. Levels of tumor necrosis factor (TNF)-α, interleukin (IL)-6, macrophage chemoattractant protein (MCP)-1, and macrophage inflammatory protein (MIP)-2 were determined in plasma and in BALF supernatants by using ELISA kits. The TNF-α, IL-6, and MCP-1 kits were from Biosource International (Camarillo, CA), and the MIP-2 kit was from TECHNE (Minneapolis, MN). The sensitivity of these kits for TNF-α, IL-6, MCP-1, and MIP-2 were 3, 3, 9, and 1.5 pg/ml, respectively, and the values were mouse specific. The absorbance of each sample was measured at 450 nm with the use of a Multiskan JX microplate reader (Thermo Labsystems, Thermo Bio-analysis, Tokyo, Japan).

Analysis of eNOS and iNOS expression. To determine the amount of NOS protein in the lung after injury, we analyzed the left lungs after lavage as previously described (22). Lung protein (50 μg) was resolved by SDS-PAGE and immunoblotted with polyclonal anti-eNOS antibody (Santa Cruz Biotechnology, Santa Cruz, CA), anti-iNOS antibody (Transduction Laboratories, Lexington, KY), and monoclonal anti-β-actin (Sigma Chemical). The eNOS antibody does not cross-react with either nNOS or iNOS.

To measure relative levels of NOS gene expression using quantitative real-time PCR, we isolated total RNA from mouse lungs with the ISOGEN reagent (Nippon Gene, Tokyo, Japan). First-strand cDNA was synthesized from 1 μg of total RNA by using ExScript RT reagent kits (Takara, Otsu, Japan) and random hexamer primers. Quantitative PCR was performed using real-time SYBR Green PCR technology and an ABI PRISM 7500 Sequence Detection system (Applied Biosystems, Foster City, CA). The primers used were as described previously (20): for iNOS: forward primer, AAG GCC ACA TCG GAT TTC AC, and reverse primer, GAT GGA CCC CAA GCA AGA CTT; and for β-actin: forward primer, CCC TAA GGC CAA CCG TGA A, and reverse primer, GTT GAA GGT CTC AAA CAT GAT CTG. Amplification reactions were performed in duplicate with SYBR Premix Ex Taq (Takara), and the thermal cycling conditions were as follows: 10 s at 95°C, 40 cycles of 5 s at 95°C, and 34 s at 60°C. Mouse iNOS and eNOS expression was normalized to β-actin mRNA expression.

NOS activity. NOS enzymatic activity was determined as the conversion of L-[^{3}H]arginine to L-[^{3}H]citrulline with saturating concentrations of substrate and cofactors (Cayman Chemical, Ann Arbor, MI) as described previously (14, 22). Ca^{2+}-dependent eNOS activity was calculated as the difference between that measured in the presence of Ca^{2+} and calmodulin and that measured in the presence of L-NAME, whereas the addition of 1 mM EGTA allowed the determination of the Ca^{2+}-independent iNOS activity. Enzyme activity was expressed as L-citrulline production in picomoles per milligram of protein per minute.

Measurement of cGMP levels in mouse lung. To determine NO release from the injured lungs, we measured cyclic guanosine 3′,5′-cyclic monophosphate (cGMP), an intracellular downstream indicator of NO release in BALF, using an enzyme immunoassay kit (Amersham BioScience, Piscataway, NJ) as described previously (22, 24). In brief, the right lungs were homogenized twice in ice-cold 6% trichloroacetic acid (TCA) and centrifuged at 2,000 rpm. The TCA in the supernatant fraction was extracted four times with H_2O-saturated diethyl ether. The samples were then lyophilized, resuspended in assay buffer, acetylated with triethylamine/acetic anhydride, and mea-

sured with a spectrophotometer. cGMP levels are expressed as picomoles per milligram of TCA-precipitable protein solubilized with 1 N NaOH.

Statistical analysis. Statistically significant differences among groups were determined using Friedman's two-way analysis of variance for multiple comparisons between groups (StatView version 4.1; ABACUS Concepts, Berkeley, CA). The VILI scores were compared using the Mann-Whitney *U*-test (Microsoft Excel, Microsoft, Tokyo, Japan). Data are expressed as means ± SE, and differences are considered statistically significant at $P < 0.05$.

RESULTS

Lung injury induced by high VT ventilation was inhibited by eNOS overexpression. We first examined lung injury induced by high VT ventilation at various times using histopathological and cytological means. Because histopathological changes and the increased proportion of neutrophils in BALF were observed 4 h after ventilation, we used this time point for all subsequent studies.

As previously reported (22), the blood pressure of eNOS-Tg mice was lower than that of WT mice (102.0 ± 9.2 vs. 119.3 ± 9.6 mmHg, respectively; $P < 0.05$, $n = 6–8$) at the beginning of MV. Over 4 h, the blood pressure of the high VT ventilation group was maintained at a lower level (81.9 ± 11.0 mmHg, $n = 6$) in eNOS-Tg mice, whereas that of the low VT group did not significantly decrease (99.4 ± 9.8 mmHg, $n = 8$). No significant difference was evident between eNOS-Tg and WT mice during MV.

The histological examination revealed no pathological differences between WT (Fig. 1*A*) and eNOS-Tg mice (Fig. 1*B*) under normal conditions without ventilation before and after ingestion of L-NAME. Compared with normal lungs from WT and eNOS-Tg mice (Fig. 1, *A* and *B*), cell infiltration in the alveolar wall and interstitial edema were obviously increased in WT mice in the high VT ventilation groups (high VT-WT) (Fig. 1*D*). On the other hand, the changes were minimal in low VT ventilation groups (low VT-WT) (Fig. 1*C*). Interestingly, such lung inflammation induced by high VT was attenuated in eNOS-Tg mice (high VT-Tg) compared with WT mice (high VT-WT) (Fig. 1, *D* vs. *E*). Moreover, the severity of the inflammatory damage in eNOS-Tg mice given the NOS inhibitor L-NAME (high VT-Tg-L-NAME) (Fig. 1*F*) was similar to that found in high VT-WT mice. L-NAME did not affect the histology of WT mice in the low and high VT as well as the nonventilated groups (data not shown).

Figure 2 shows the histopathological grades of VILI using the scoring system described in METHODS (2). The VILI scores were significantly increased in high VT-WT mice compared with WT and low VT-WT mice. In contrast, the scores in high VT-Tg mice were significantly lower than those in the high VT-WT group. Moreover, L-NAME (high VT-Tg-L-NAME) led to a higher score than that of high VT-Tg mice, whereas high VT-WT and high VT-WT-L-NAME mice did not differ. These findings suggest that eNOS overexpression in the lungs inhibits the development of VILI.

Airway neutrophil inflammation was attenuated in eNOS-Tg mice. The BALF from untreated WT and eNOS-Tg mice contained exclusively alveolar macrophages. High VT ventilation significantly increased total cell counts in BALF from WT mice (high VT-WT) (Fig. 3*A*). However, the high VT ventilation-induced inflammatory cell infiltration was completely attenuated by eNOS overexpression (high VT-Tg). Treating high VT-Tg mice with L-NAME (high VT-Tg-L-NAME group) increased the total cell counts compared with high VT-Tg mice,

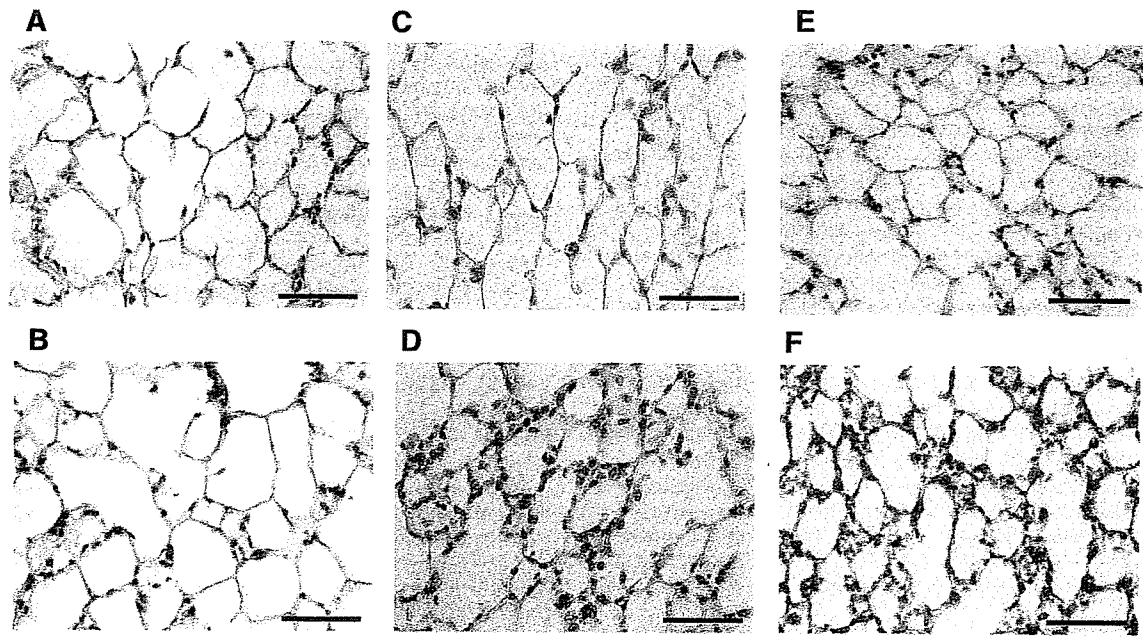

Fig. 1. Hematoxylin and eosin-stained lung sections. *A* and *B*: normal lungs of wild-type (WT) (*A*) and endothelial nitric oxide synthase-transgenic (eNOS-Tg) mice (*B*) without ventilation. *C* and *D*: WT mouse lungs ventilated with low tidal volume (low VT-WT; *C*) and high tidal volume (high VT-WT; *D*). *E* and *F*: Tg mouse lungs ventilated with high VT in the absence (high VT-Tg; *E*) or presence of N^{ω}-nitro-L-arginine methyl ester (high VT-Tg-L-NAME; *F*). Magnification, ×400. Bars, 50 μm.

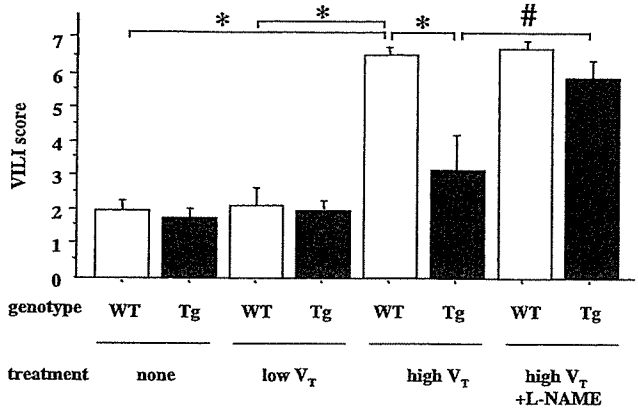

Fig. 2. Semiquantitative analysis of ventilator-induced lung injury (VILI). VILI scores are based on leukocyte infiltration, exudative edema, hemorrhage, and alveolar wall thickness as described in METHODS. Values are means ± SE of at least 5 mice per group. *$P < 0.0001$; #$P < 0.001$.

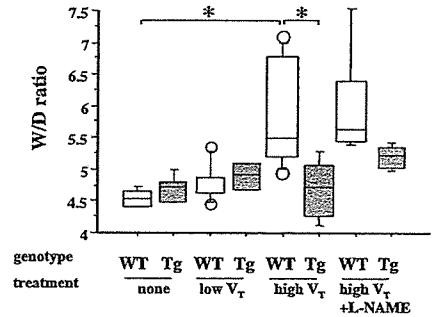

Fig. 4. Lung water content after VILI. The ratio of wet to dry weight (W/D) of lungs was determined in right whole lungs by dividing wet weight by dry weight. Values are means ± SE of at least 6 mice per group. *$P < 0.0001$.

but the increase was not statistically significant. High VT-Tg-L-NAME and high VT-WT-L-NAME mice did not differ.

The high VT ventilation significantly increased neutrophil infiltration in BALF in both WT and eNOS-Tg mice (Fig. 3*B*). The ratio (%) of neutrophils to total cells was significantly higher in high VT-WT mice. Moreover, this neutrophil infiltration was significantly decreased in high VT-Tg mice (Fig. 3*B*). When the high VT-Tg mice were treated with L-NAME, however, the neutrophil proportion in high VT-Tg mice was similar to that in high VT-WT mice. These data indicate that the high VT ventilation-induced neutrophil infiltration in the airway was inhibited by eNOS overexpression.

Increases in lung edema after VILI were reduced in eNOS-Tg mice. Lung edema induced by acute lung inflammation was evaluated using the lung W/D ratio. This ratio did not significantly differ between the low VT ventilation WT and eNOS-Tg groups. However, high VT ventilation evoked severe lung edema in WT mice (high VT-WT), whereas the same procedure in eNOS-Tg mice (high VT-Tg) did not induce significant lung edema (Fig. 4). The lung W/D ratio after L-NAME treatment was not altered in high VT-WT mice but increased in high VT-Tg mice. Consequently, the water content of the lungs in high VT-Tg mice was similar to that in high VT-WT mice when the mice were treated with L-NAME. These data indicate that the lung edema induced by high VT ventilation was inhibited by eNOS overexpression.

Lung eNOS expression and activity were increased in eNOS-Tg mice. We previously localized eNOS overexpression in pulmonary airway and alveolar cells as well as in the endothelium of pulmonary arteries and veins of eNOS-Tg mice (22). Consistent with these results, eNOS protein levels in the lungs of eNOS-Tg mice were significantly higher than those in WT mice (Fig. 5*A*). Notably, high VT ventilation did not change the eNOS protein level in the lungs of WT and eNOS-Tg mice. Similarly, the eNOS levels were not increased in mice given L-NAME, regardless of ventilation. On the other hand, the amount of iNOS protein was not significantly increased in this model even after MV, and quantitative PCR confirmed that iNOS mRNA was not induced by the MV, in contrast to the marked iNOS induction by LPS (Fig. 5*B*).

We then examined NOS activity as the conversion assay of L-arginine to L-citrulline (Fig. 5*C*). Ca^{2+}-dependent eNOS

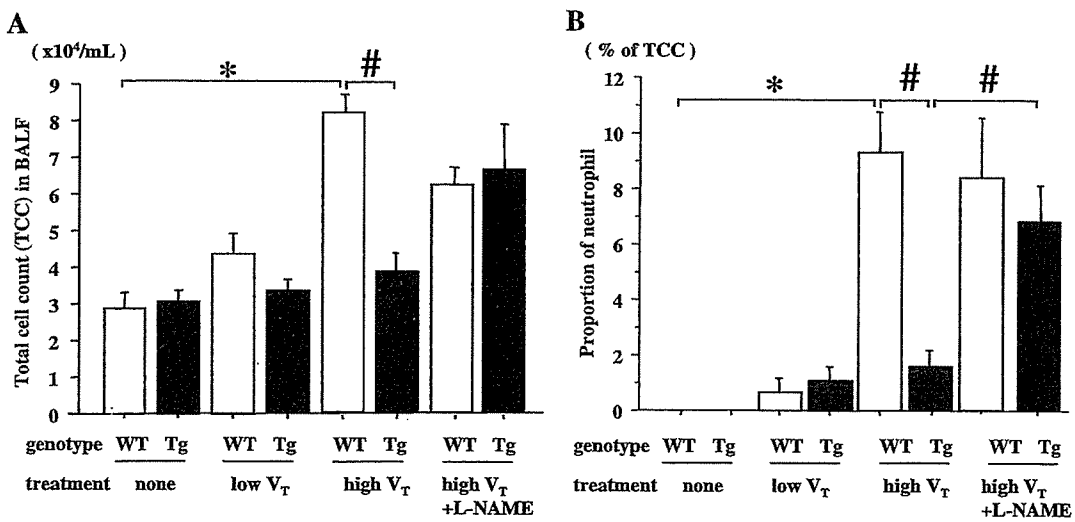

Fig. 3. Bronchoalveolar lavage fluid (BALF) analysis in VILI. *A*: total cell count (TCC). *B*: neutrophil cells as a ratio (%) of TCC in BALF. After mechanical ventilation (MV), BALF was obtained and examined using Diff Quik staining. Values are means ± SE of at least 5 mice per group. *$P = 0.0005$; #$P < 0.05$.

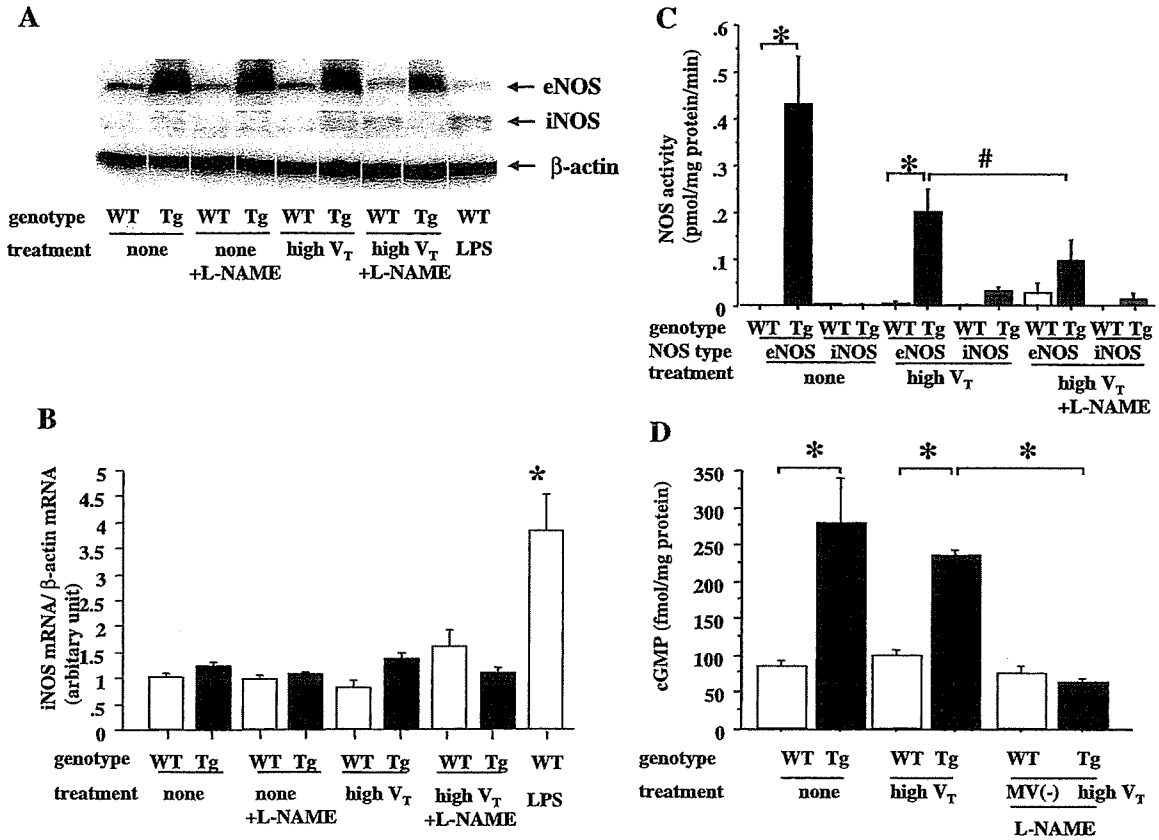

Fig. 5. Expression and activity of eNOS and inducible NOS (iNOS) in mouse lungs. *A*: Western blots were used to detect eNOS, iNOS, and β-actin protein in lung homogenates. *B*: quantitative PCR was used to determine mRNA levels of iNOS. *C*: conversion of L-[^{3}H]arginine to L-[^{3}H]citrulline was used to determine NOS activity, shown as Ca^{2+}-dependent (eNOS, open bars) and -independent activity (iNOS, solid bars). *D*: cGMP levels in lung homogenates were determined using enzyme immunoassay. Values are means ± SE of 5 mice per group. $*P < 0.005$; $\#P < 0.05$.

activity was easily detected in eNOS-Tg mice and was inhibited by L-NAME. In contrast, Ca^{2+}-independent iNOS activity was not significantly increased by the ventilation procedures in either mouse group. Similarly, cGMP analysis revealed that eNOS-Tg mice had two- to threefold higher basal cGMP levels than WT mice, and the MV procedure did not augment the cGMP accumulation (Fig. 5*D*). These findings suggest that our MV procedure did not stimulate iNOS induction in mice.

Cytokine levels in plasma and BALF were reduced in eNOS-Tg mice. Injurious ventilatory strategies increase the concentrations of various inflammatory cytokines (30), and among these, we measured IL-6 and TNF-α levels as markers of inflammation (Fig. 6). Both TNF-α and IL-6 levels were increased by high VT ventilation in BALF and plasma, although IL-6 values in BALF did not significantly differ between WT and eNOS-Tg mice. On the other hand, the increased TNF-α level in the plasma of high VT-WT mice (446.5 ± 174.7 pg/ml, $P < 0.001$ vs. WT) was significantly reduced in high VT-Tg mice (59.2 ± 12.8 pg/ml, $P < 0.0001$ vs. high VT-WT), and the finding was similar in BALF. L-NAME (high VT-Tg-L-NAME) slightly increased the plasma level of IL-6 and TNF-α compared with the high VT-Tg group, whereas no significant change was evident in WT mice given L-NAME (high VT-WT-L-NAME). That is, IL-6 and TNF-α levels in plasma and BALF did not significantly differ between WT and eNOS-Tg mice in the presence of L-NAME.

Figures 7*A* and 8*A* show that MIP-2 concentrations were significantly increased in high VT-WT mice (326.1 ± 84.9 pg/ml in BALF and 1,808.5 ± 320.9 pg/ml in plasma) compared with in WT mice ($P < 0.005$). These increases were appreciably attenuated in high VT-Tg mice (59.1 ± 14.7 pg/ml in BALF and 178.9 ± 80.0 pg/ml in plasma) compared with high VT-WT ($P < 0.001$). This attenuation was abolished by L-NAME only in eNOS-Tg mice (314.9 ± 80.1 pg/ml in BALF and 1,479.0 ± 326.8 pg/ml in plasma). Furthermore, the plasma concentration profile of MCP-1 (Fig. 8*B*) was similar to that of MIP-2. Under high VT ventilation, the plasma level of MCP-1 was significantly increased in high VT-WT mice (2,252.7 ± 527.8 pg/ml, $P < 0.001$ vs. WT) and attenuated in high VT-Tg mice (254.9 ± 82.1 pg/ml, $P < 0.001$ vs. high VT-WT). On the other hand, BALF levels of MCP-1 were increased in high VT-WT mice, although the difference was not statistically significant ($P = 0.099$ vs. WT, Fig. 7*B*).

DISCUSSION

The present study demonstrated that MV with a high VT caused lung edema and inflammation in mice, which was accompanied by cytokine/chemokine release. In contrast, a low VT caused only minimal histological damage to the lungs. These tidal volume-dependent lung injuries in humans have been documented, where the low and high VT is related to the

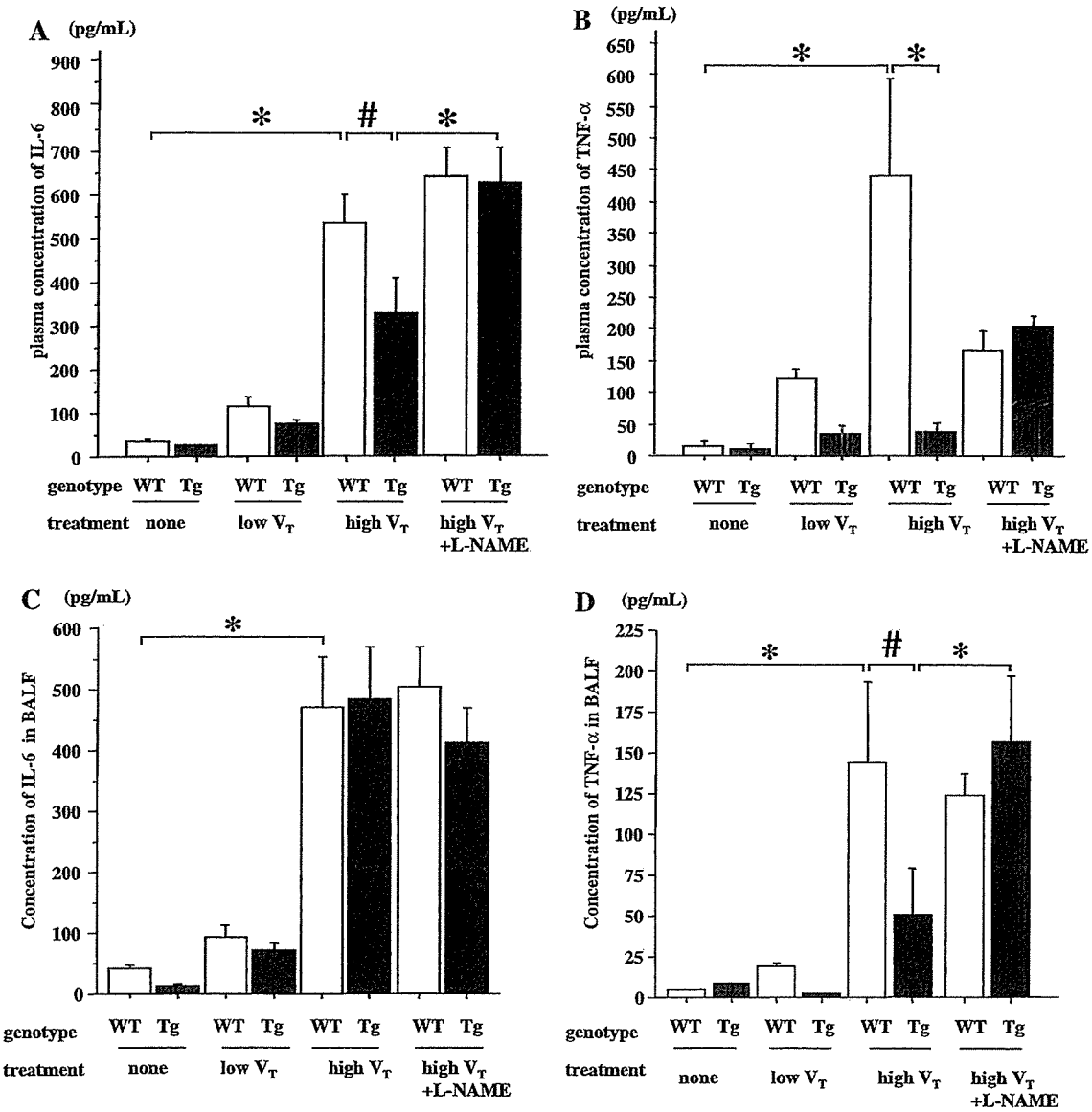

Fig. 6. Cytokine levels in plasma (*A* and *B*) and BALF (*C* and *D*) measured using ELISA after MV. Both cytokine levels in plasma were lower in high V_T-Tg than in high V_T-WT mice. BALF levels of IL-6 (*C*) were not affected by eNOS overexpression, whereas those of TNF-α (*D*) were decreased in high V_T-Tg mice (n = 6–8 mice per group). Values are means ± SE of five mice per group. *$P < 0.005$; #$P < 0.05$.

protective and conventional strategy, respectively, in agreement with the clinical study reported by the ARDS network (1). Our VILI scoring system confirmed that the histopathological grading of VILI closely matched the degree of tidal volume.

One of the major findings of this study was that the high V_T-induced lung injury was inhibited in eNOS-Tg mice. Although it is widely accepted that NO modulates inflammation through a variety of mechanisms (15, 19) and NO is produced by several NOS isoforms, the relative contribution of these isoforms in inflammation has not been defined. Several animal models have been established to characterize the role of NOS in lung inflammation (6, 11, 14, 21). For instance, chemicals such as LPS evoke lung injury, but defining the role of eNOS in the chemically induced lung injury model is difficult, because endotoxin exposure directly activates iNOS. In the present study, we found that iNOS levels were not affected by the MV procedure in mice, which is consistent with the results of a previous study showing that that MV does not induce iNOS expression in rats (6). The NOS activity assay confirmed that the MV procedure did not stimulate Ca^{2+}-independent iNOS activity. Furthermore, the effect of eNOS overexpression was reversed by L-NAME. From these results, we concluded that the reduction of VILI in eNOS-Tg mice was mainly caused by NO derived from overexpressed eNOS in the lung.

On the other hand, a recent study by Peng et al. (25) showed that iNOS may be an important contributor to VILI and that iNOS protein was increased after 2-h MV. We could not

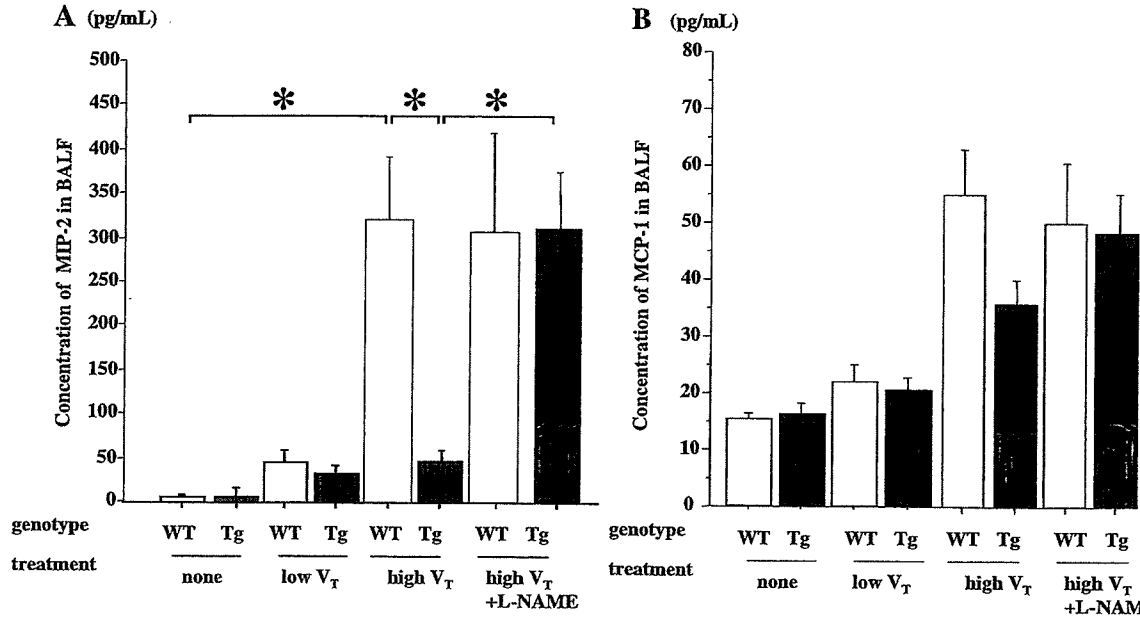

Fig. 7. Macrophage inflammatory protein (MIP)-2 and macrophage chemoattractant protein (MCP)-1 concentrations in BALF. Release of MIP-2 (*A*) and MCP-1 (*B*) into BALF after MV was evaluated using ELISA (n = 6–8 mice per group). The concentration of MIP-2 was increased by MV (high VT-WT) and obviously reduced in high VT-Tg. The concentration of MCP-1 tended to increase similarly to MIP-2, but the difference was not statistically significant. Values are means ± SE of 5 mice per group. *$P < 0.01$.

resolve the discrepancy of iNOS expression in VILI; however, there are many methodological differences in the ventilation protocol as described in the article. We speculate that our blood pressure monitoring without a cannulation procedure might cause some influence on the data, and our present study is similar to that described by Hammerschmidt et al. (9) in which high VT ventilation reduced eNOS gene expression but did not affect iNOS expression in isolated rabbit lungs.

It has been postulated that eNOS-derived NO plays a protective role against lung injury. MacRitchie et al. (21) showed that decreased eNOS protein expression in both pulmonary artery and airways is associated with lung injury in preterm lambs ventilated for 3 wk. Furthermore, eNOS-deficient mice are susceptible to severe lung edema and inflammation after ischemia-reperfusion injury (11). These findings, together with our present data, have strengthened the notion that NO derived from chronic eNOS overexpression may protect the lung from VILI.

Several plausible mechanisms could explain the reduced VILI in eNOS-Tg mice. First, NO derived from eNOS could

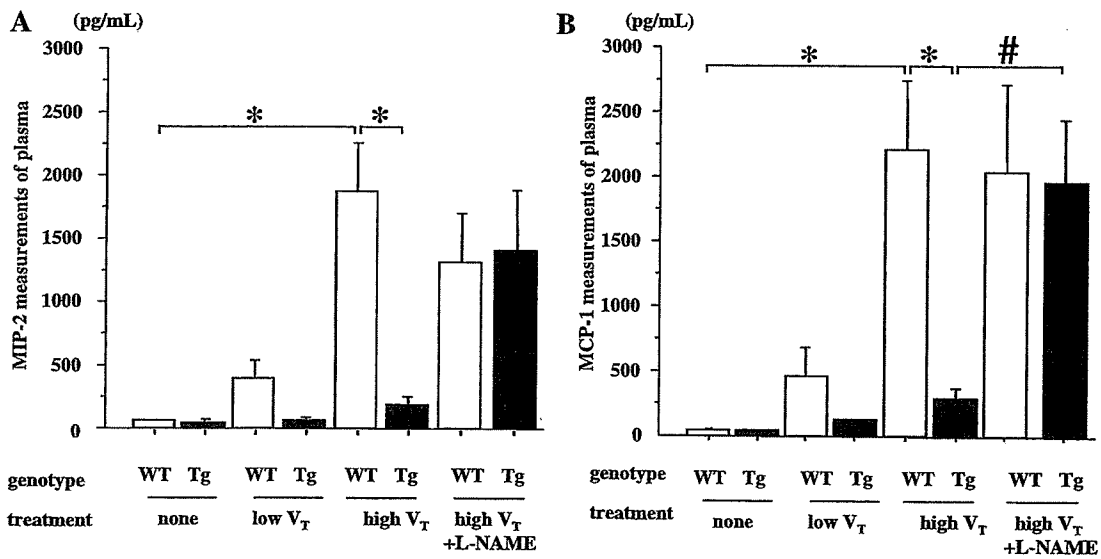

Fig. 8. MIP-2 and MCP-1 concentrations in plasma. Release of MIP-2 (*A*) and MCP-1 (*B*) into plasma after MV was measured using ELISA (n = 6–8 mice per group). Concentrations of MIP-2 and MCP-1 were significantly elevated in high VT-WT mice and obviously attenuated in high VT-Tg mice. Values are means ± SE of 5 mice per group. *$P < 0.001$; #$P < 0.005$.

inhibit neutrophil infiltration and macrophage activation. Activated macrophages respond immediately to the overdistension of alveolar tissue, attract neutrophils by releasing proinflammatory cytokines, and play an important role in initiating the inflammation associated with VILI (10). Kawano et al. (12) found that the diffuse infiltration by activated neutrophils was induced by MV in the rabbit lung, whereas lung damage was minimal in neutrophil-depleted animals. Our observation also supports the evidence that neutrophils are one of the key regulators during the pathogenesis of VILI.

Second, NO could alter cytokine/chemokine release and receptor expression in the lung. Proinflammatory cytokines and chemokines are produced during injurious ventilation and ALI/ARDS (30). For instance, the CXC chemokines (MIP-2, KC) attract neutrophils into the lung, whereas CC chemokines (MCP-1, MCP-3) attract lymphocytes and monocytes and activate macrophages (23). Belperio et al. (2) demonstrated that KC/CXCL1 and MIP-2/CXCL2/3, through interaction with their shared receptor, CXC chemokine receptor 2 (CXCR2), regulates neutrophil recruitment by promoting neutrophil adherence to endothelial cells and transendothelial migration into lung tissue. On the other hand, cell surface expression of CXCR2 is increased on nonleukocyte cell populations in the high V_T group (31). These findings imply that mechanical stimulation of nonleukocytes upregulates chemokine receptor expression by fibroblasts as well as by epithelial and endothelial cells, which play a significant role in mediating VILI via neutrophil recruitment.

The present study found that both TNF-α and IL-6 levels were increased by high V_T ventilation in BALF and plasma and that the expression was decreased in eNOS-Tg mice. The concentration of TNF-α in BALF was similar to that of plasma, but the change in TNF-α was more significant in plasma. These data suggest that VILI caused systemic injury and imply that plasma TNF-α levels may be more sensitive to lung injury. The overexpression of eNOS also reduced MIP-2 release after MV. Moreover, MCP-1 levels were decreased in high V_T-Tg compared with high-WT mice, especially in plasma. These molecules are important mediators of lung inflammation by interaction with NO (3, 29, 32, 36). On the other hand, NO blocks the upregulation of adhesion molecules such as VCAM-1 (7), ICAM-1, and P-selectin (17). We did not show evidence that our VILI model affects these adhesion molecule expressions in this study; however, these facts suggested that the inhibition of inflammatory cytokines and adhesion molecules by overproduction of NO might play some roles in hematopoietic-endothelial cell interaction in the pathogenesis of VILI.

The anti-inflammatory effect of NO might be useful in a therapeutic environment. Inhaled NO reduces lung inflammation and injury in premature lambs that receive MV for 3 h after birth (13). Inhaled NO is now used clinically to treat acute lung injury in humans (31), although a beneficial effect on survival has not yet been established. Our study found that eNOS was chronically overexpressed mainly in vascular endothelial cells, and we showed that NO derived from endothelial cells inhibited neutrophil-associated lung edema and inflammation by reducing cytokine/chemokine production in VILI. These data support previous findings indicating that NO may help to prevent VILI. However, the clinical effect and approach of eNOS delivery have not been established and should be evaluated by further studies.

ACKNOWLEDGMENTS

We thank Dr. Chiho Obayashi (Department of Pathology, Kobe University Graduate School of Medicine) for helpful advice during the histopathological analyses.

REFERENCES

1. **The Acute Respiratory Distress Syndrome Network.** Ventilation with lower tidal volume as compared with traditional tidal volumes for acute lung injury and the acute respiratory distress syndrome. *N Engl J Med* 342: 1301–1308, 2000.
2. **Belperio JA, Keane MP, Burdick MD, Londhe V, Xue YY, Li K, Phillips RJ, and Strieter RM.** Critical role for CXCR2 and CXCR2 ligands during the pathogenesis of ventilator-induced lung injury. *J Clin Invest* 110: 1703–1716, 2002.
3. **Bethmann AN von, Brasch F, Nusing R, Vogt K, Volk HD, Muller KM, Wendel A, and Uhlig S.** Hyperventilation induces release of cytokines from perfused mouse lung. *Am J Respir Crit Care Med* 157: 263–272, 1998.
4. **Bogdan C.** Nitric oxide and the immune response. *Nat Immunol* 2: 907–916, 2001.
5. **Chiumello D, Pristine G, and Slutsky AS.** Mechanical ventilation affects local and systemic cytokines in an animal model of acute respiratory distress syndrome. *Am J Respir Crit Care Med* 160: 109–116, 1999.
6. **Choi WI, Quinn DA, Park KM, Moufarrej RK, Jafari B, Syrkina O, Bonventre JV, and Hales CA.** Systemic microvascular leak in an in vivo rat model of ventilator-induced lung injury. *Am J Respir Crit Care Med* 167: 1627–1632, 2003.
7. **De Caterina R, Libby P, Peng HB, Thannickal VJ, Rajavashisth TB, Gimbrone MA Jr, Shin WS, and Liao JK.** Nitric oxide decreases cytokine-induced endothelial activation: nitric oxide selectively reduces endothelial expression of adhesion molecules and proinflammatory cytokines. *J Clin Invest* 96: 60–68, 1995.
8. **Dreyfuss D and Saumon G.** Ventilator-induced lung injury: lessons from experimental studies. *Am J Respir Crit Care Med* 157: 294–323, 1998.
9. **Hammerschmidt S, Schiller J, Kuhn H, Meybaum M, Gessner C, Sandvoss T, Arnold K, and Wirtz H.** Influence of tidal volume on pulmonary NO release, tissue lipid peroxidation and surfactant phospholipids. *Biochim Biophys Acta* 1639: 17–26, 2003.
10. **Imanaka H, Shimaoka M, Matsuura N, Nishimura M, Ohta N, and Kiyono H.** Ventilator-induced lung injury is associated with neutrophil infiltration, macrophage activation, and TGF-β1 mRNA upregulation in rat lungs. *Anesth Analg* 92: 428–436, 2001.
11. **Kaminski A, Pohl CB, Sponholz C, Ma N, Stamm C, Vollmar B, and Steinhoff G.** Up-regulation of endothelial nitric oxide synthase inhibits pulmonary leukocyte migration following lung ischemia-reperfusion in mice. *Am J Pathol* 164: 2241–2249, 2004.
12. **Kawano T, Mori S, Cybulsky M, Burger R, Ballin A, Cutz E, and Bryan AC.** Effect of granulocyte depletion in a ventilated surfactant-depleted lung. *J Appl Physiol* 62: 27–33, 1987.
13. **Kinsella JP, Parker TA, Galan H, Sheridan BC, Halbower AC, and Abman SH.** Effects of inhaled nitric oxide on pulmonary edema and lung neutrophil accumulation in severe experimental hyaline membrane disease. *Pediatr Res* 41: 457–463, 1997.
14. **Kristof AS, Goldberg P, Laubach V, and Hussain SN.** Role of inducible nitric oxide synthase in endotoxin-induced acute lung injury. *Am J Respir Crit Care Med* 158: 1883–1889, 1998.
15. **Kubes P, Suzuki M, and Granger DN.** Nitric oxide: an endogenous modulator of leukocyte adhesion. *Proc Natl Acad Sci USA* 88: 4651–4655, 1991.
16. **Kubes P and Granger DN.** Nitric oxide modulates microvascular permeability. *Am J Physiol Heart Circ Physiol* 262: H611–H615, 1992.
17. **Kubes P, Kurose I, and Granger DN.** NO donors prevent integrin-induced leukocyte adhesion but not P-selectin-dependent rolling in postischemic venules. *Am J Physiol Heart Circ Physiol* 267: H931–H937, 1994.
18. **Kubes P.** Nitric oxide affects microvascular permeability in the intact and inflamed vasculature. *Microcirculation* 2: 235–244, 1995.
19. **Kurose I, Kubes P, Wolf R, Anderson DC, Paulson J, Miyasaka M, and Granger DN.** Inhibition of nitric oxide production: mechanisms of vascular albumin leakage. *Circ Res* 73: 164–171, 1993.
20. **Lee JK, Borhani M, Ennis TL, Upchurch GR Jr, Thompson RW.** Experimental abdominal aortic aneurysms in mice lacking expression of inducible nitric oxide synthase. *Arterioscler Thromb Vasc Biol* 21: 1393–401, 2001.

21. **MacRitchie AN, Albertine KH, Sun J, Lei PS, Jensen SC, Freestone AA, Clair PM, Dahl MJ, Godfrey EA, Carlton DP, and Bland RD.** Reduced endothelial nitric oxide synthase in lungs of chronically ventilated preterm lambs. *Am J Physiol Lung Cell Mol Physiol* 281: L1011–L1020, 2001.
22. **Ohashi Y, Kawashima S, Hirata K, Yamashita T, Ishida T, Inoue N, Sakoda T, Kurihara H, Yazaki Y, and Yokoyama M.** Hypotension and reduced nitric oxide-elicited vasorelaxation in transgenic mice overexpressing endothelial nitric oxide synthase. *J Clin Invest* 102: 2061–2071, 1998.
23. **Olson TS and Ley K.** Chemokines and chemokine receptors in leukocyte trafficking. *Am J Physiol Regul Integr Comp Physiol* 283: R7–R28, 2002.
24. **Ozaki M, Kawashima S, Yamashita T, Ohashi Y, Rikitake Y, Inoue N, Hirata K, Hayashi Y, Itoh H, and Yokoyama M.** Reduced hypoxic pulmonary vascular remodeling by nitric oxide from the endothelium. *Hypertension* 37: 322–327, 2001.
25. **Peng X, Abdulnour RE, Sammani S, Ma SF, Han EJ, Hasan EJ, Tuder R, Garcia JG, and Hassoun PM.** Inducible nitric oxide synthase contributes to ventilator-induced lung injury. *Am J Respir Crit Care Med* 172: 470–479, 2005.
26. **Pinhu L, Whitehead T, Evans T, and Griffiths M.** Ventilator-associated lung injury. *Lancet* 361: 332–340, 2003.
27. **Quinn DA, Moufarrej RK, Volokhov A, and Hales CA.** Interactions of lung stretch, hyperoxia, and MIP-2 production in ventilator-induced lung injury. *J Appl Physiol* 93: 517–525, 2002.
28. **Skidgel RA, Gao XP, Brovkovych V, Rahman A, Jho D, Predescu S, Standiford TJ, and Malik AB.** Nitric oxide stimulates macrophage inflammatory protein-2 expression in sepsis. *J Immunol* 169: 2093–2101, 2002.
29. **Sokol J, Jacobs SE, and Bohn D.** Inhaled nitric oxide for acute hypoxic respiratory failure in children and adults: a meta-analysis. *Anesth Analg* 97: 989–998, 2003.
30. **Tremblay L, Valenza F, Ribeiro SP, Li J, and Slutsky AS.** Injurious ventilatory strategies increase cytokines and c-*fos* m-RNA expression in an isolated rat lung model. *J Clin Invest* 99: 944–952, 1997.
31. **Tremblay LN, Miatto D, Hamid Q, Govindarajan A, and Slutsky AS.** Injurious ventilation induces widespread pulmonary epithelial expression of tumor necrosis factor-α and interleukin-6 messenger RNA. *Crit Care Med* 30: 1693–1700, 2002.
32. **Uhlig S.** Ventilation-induced lung injury and mechanotransduction: stretching it too far? *Am J Physiol Lung Cell Mol Physiol* 282: L892–L896, 2002.
33. **Ware LB and Matthay MA.** The acute respiratory distress syndrome. *N Engl J Med* 342: 1334–1349, 2000.
34. **Wilson MR, Choudhury S, Goddard ME, O'Dea KP, Nicholson AG, and Tanaka M.** High tidal volume ventilation upregulates intrapulmonary cytokines in an in vivo mouse model of ventilator-induced lung injury. *J Appl Physiol* 95: 1385–1393, 2003.
35. **Yamashita T, Kawashima S, Ohashi Y, Ozaki M, Ueyama T, Ishida T, Inoue N, Hirata K, Akita H, and Yokoyama M.** Resistance to endotoxin shock in transgenic mice overexpressing endothelial nitric oxide synthase. *Circulation* 101: 931–937, 2000.
36. **Zeiher AM, Fisslthaler B, Schray-Utz B, and Busse R.** Nitric oxide modulates the expression of monocyte chemoattractant protein 1 in cultured human endothelial cells. *Circ Res* 76: 980–986, 1995.

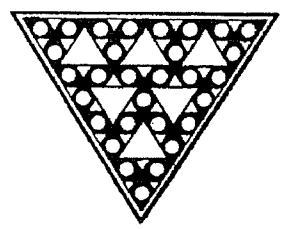

An X-Ray Diffraction Study on Mouse Cardiac Cross-Bridge Function In Vivo: Effects of Adrenergic β-Stimulation

Ryuji Toh,* Masakazu Shinohara,* Tomofumi Takaya,* Tomoya Yamashita,* Shigeru Masuda,* Seinosuke Kawashima,* Mitsuhiro Yokoyama,* and Naoto Yagi†

*Division of Cardiovascular and Respiratory Medicine, Department of Internal Medicine, Kobe University Graduate School of Medicine, Kobe 650-0017, Japan; and †SPring-8/JASRI, Sayo, Hyogo 679-5198, Japan

ABSTRACT To investigate how β-stimulation affects the contractility of cardiac muscle, x-ray diffraction from cardiac muscle in the left ventricular free wall of a mouse heart was recorded in vivo. To our knowledge, this is the first x-ray diffraction study on a heart in a living body. After the R wave in electrocardiograms, the ratio of the intensities of the equatorial (1,0) and (1,1) reflections decreased for ~50 ms from a diastolic value of 2.1 to a minimum of 0.8, and then recovered. The spacing of the (1,0) lattice planes increased for ~90 ms from a diastolic value of 37.2 nm to a maximum of 39.1 nm, and then returned to the diastolic level, corresponding to ~10% stretch of sarcomere. Stimulation of β-adrenergic receptor by dobutamine (20 μg/kg/min) accelerated both the decrease in the intensity ratio, which reached a smaller systolic value, and the increase in the lattice spacing. However, the intensity ratio and spacing at the end-diastole were unchanged. The recovery of the lattice spacing during relaxation was also accelerated. The mass transfer to the thin filaments at systole in a β-stimulated heart was close to the peak value in twitch of frog skeletal muscle at 4°C, showing that the majority of cross-bridges have been recruited with few in reserve.

INTRODUCTION

Stimulation of cardiac β-adrenergic receptors has been known to enhance contractility of cardiac muscle through phosphorylation of various enzymes, including troponin-I, C-protein, and phospholamban (1–6). Although these effects have been extensively studied both physiologically and biochemically in isolated cardiac muscles and myocytes, they can be studied in a living body by only a limited number of methods. Lack of a molecular index that can be measured in vivo has made it difficult to study the mechanism of the β-stimulation. Since the overall influence of neurohumoral factors on functional properties of cardiac muscle can only be studied in vivo, it is important to develop a method to monitor contractility at the molecular level in a live animal. This is especially important when investigating the consequences of genetic alterations.

It is usually difficult to study murine, especially mouse, cardiac muscle in an isolated specimen under physiological conditions. Perfusion with oxygenated saline does not provide enough oxygen, and a heart tends to be in a hypoxic condition at physiological heart rates. Although an x-ray diffraction study on an intact rat papillary muscle has the advantage that force and sarcomere length can be measured simultaneously, such experiments have been made at a heart rate lower than 1 Hz (7,8). Since the heart rate is an important factor in cardiac physiology, which affects calcium handling and contractile force, it is necessary to make these experiments at higher heart rates. This is especially the case if the increase in the contractile force with increased heart rate (the staircase phenomenon) is due to a higher number of cross-bridges associated with the thin filament during diastole (9).

X-ray diffraction has been used to study contractility of cardiac muscle. It is a noninvasive method which enables us to study myosin cross-bridge activity in striated muscles (10). Two pieces of information can be obtained: one is the intensity ratio of the (1,0) and (1,1) equatorial reflections from the hexagonal lattice of myofilaments, which can be used as an index of the number of myosin cross-bridges formed during contraction (mass transfer from the thick to the thin filament). This correlates well with tension development in cardiac muscle, especially during the early phase of contraction under an isometric condition (9). Theoretically, the intensity ratio might be affected by a conformational change of cross-bridges. However, experiments on skeletal muscle showed that a force-generating conformational change does not affect the ratio (11). Thus, the change in the ratio is mostly caused by a mass movement from the thick filaments to the thin filaments due to cross-bridge formation. The other piece of available information is the (1,0) spacing of the lattice, which is equal to $\sqrt{3}/2$ of the distance between neighboring thick filaments. Since the volume of a cardiac cell remains approximately constant during a cardiac cycle (7), the lattice spacing can be used as an index of sarcomere length.

Recently, it was shown that diffraction patterns from a whole heart can be interpreted based on the orientation of muscle fibers in the heart (12), and a time-resolved x-ray diffraction study was made on a heart of a thoractomized rat (13). Here we applied this technique to a heart in a body of a

Submitted September 8, 2005, and accepted for publication November 18, 2005.

Ryuji Toh and Masakazu Shinohara contributed equally to this article.

Address reprint requests to N. Yagi, SPring-8/JASRI, Kouto, Sayo, Hyogo 679-5198, Japan. Tel.: 81-791-58-0908; Fax: 81-791-58-0830; E-mail: yagi@spring8.or.jp.

0006-3495/06/03/1723/06 $2.00

doi: 10.1529/biophysj.105.074062

living mouse to study physiological functions of myosin cross-bridges in vivo. Without thoractomizing, this is the first time the contractility in heart muscle was studied at a molecular level in a living body. Effects of β-stimulation by dobutamine were investigated.

METHODS

Animal preparation

Eight-week-old male mice (C57BL/6, purchased from CLEA Japan, Tokyo, Japan) were anesthetized with isoflurane (0.25–0.5%) and artificially ventilated (MiniVent, Hugo Sachs Elektronik, March-Hugstetten, Germany; stroke volume 200 μl, 250 strokes/min). To avoid strong x-ray diffraction spots from skeletal muscles (see below), part of the breast muscles was surgically removed. The mouse was fixed vertically in the x-ray beam, which entered the thorax from the third intercostal space. In this configuration, the x-ray beam passed through the upper part of the left ventricle, whose motion during a heart beat is smaller than in the lower part. The electrocardiogram was recorded with three electrodes (Fig. 1). Systemic blood pressure was measured by a computerized tail-cuff apparatus (MK-2000, Muromachi Kikai, Tokyo, Japan). The ventilator was stopped during an x-ray exposure (for ~2 s) to avoid movement due to respiration. Dobutamine was infused from carotid artery at a rate of 20 μg/kg/min. The animal experiments were conducted in accordance with the guidelines of SPring-8 for care and welfare of experimental animals.

X-ray diffraction methods

X-ray diffraction experiments were conducted at BL40XU in the SPring-8 third generation synchrotron radiation facility (Harima, Hyogo, Japan) (14). The peak x-ray energy was adjusted to 15.0 keV. This high energy ensured sufficient penetration of x-rays through the body of a mouse. The x-ray flux was adjusted by the front-end slits and aluminum absorbers to $\sim 3 \times 10^{12}$ photons/s. The beam size was ~0.10 mm vertically, 0.25 mm horizontally at the specimen.

The x-ray detector was an x-ray image intensifier with a beryllium window (V5445P, Hamamatsu Photonics, Hamamatsu, Japan) (15) coupled by a tandem lens to a fast charge-coupled device (CCD) camera (C4880-80-24A, Hamamatsu Photonics). The time resolution was 15 ms/frame. An x-ray shutter was opened for 1.1 s, and 70 successive frames were recorded.

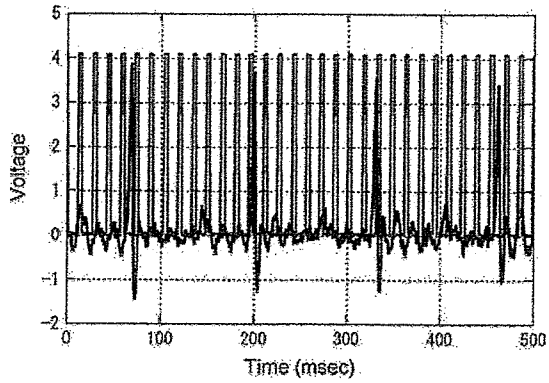

FIGURE 1 Electrocardiogram (*blue*) and frame timing of the CCD camera (*red*) during time-resolved x-ray recording. There is noise in the electrocardiogram from the power line (60 Hz) but sharp QRS peaks and preceding small Q peaks are clearly seen. The rising edge of the frame timing pulses corresponds to the beginning of a new frame.

The specimen-to-detector distance was 3.2 m. The lattice spacing was calibrated with the third-order meridional reflection from the thick filament of frog skeletal muscle at 1/14.34 nm^{-1}. Both the electrocardiogram and the frame timing signal from the CCD camera were recorded with a data acquisition system with 1-ms sampling.

Experimental protocol

Since there are layers of skeletal muscles in the path of the x-ray beam, diffraction patterns from a mouse heart in vivo are always mixed with equatorial diffraction spots from skeletal muscles. With a mouse positioned vertically and an x-ray beam passing between the third and fourth ribs, usually two sets of spots were found in the directions of 10 o'clock and 4 o'clock, and 9 o'clock and 3 o'clock (Fig. 2). The areas between these spots were free from reflections due to skeletal muscles. Initially, the x-ray beam was positioned in the left side of a mouse thorax (Fig. 3, position *A*). Then, the mouse was moved across the beam horizontally so that its left ventricular free wall came into the beam (Fig. 3, position *B*). When the x-ray beam passed through the epicardium of the free wall, the equatorial reflections, which appear as spots (12), were observed in the directions similar to those of skeletal muscles. Thus, the epicardium surface plane seems to be approximately vertical in the mouse body. At this position, the movement of the heart due to beating shifted the heart in and out of the beam in every heart beat, making it impossible to observe the diffraction pattern continuously. When the mouse was moved further and the x-ray beam passed through the deeper layer of the free wall (Fig. 3, position *C*), the equatorial diffraction pattern became arcs (12). At this stage, it was still difficult to observe the diffraction pattern continuously because the beam passed through different regions of the wall in diastole and systole. When the mouse was moved further in the beam (Fig. 3, position *D*), the diffraction pattern appeared as a ring or a long arc with maximum intensity in the direction perpendicular to the diffraction from skeletal muscles (Fig. 2). The diffraction pattern was continuously observed during a heart beat, allowing us to study the molecular changes throughout a cardiac cycle. Thus, experiments were made under this condition. The x-ray beam is presumed to be passing through endocardium and left ventricle (12). Marking the recorded region after an experiment, with an x-ray flux three orders of magnitude higher than that used for the x-ray diffraction measurement, confirmed that the beam actually passed through the left ventricular free wall.

The x-ray recording was repeated up to 10 times (average 5.3 recordings) with a horizontal shift of a mouse by 0.2 mm. The data were analyzed only when distinct diffraction from cardiac muscle was observed throughout a cardiac cycle. After dobutamine infusion, the mouse was moved vertically by ~0.2 mm to avoid radiation damage, and the recordings were repeated. No sign of radiation damage, such as broadening or weakening of the equatorial intensity profile, was seen.

Since the x-ray recording was not in synchrony with the cardiac cycle, it was necessary to determine correspondence between the x-ray frames and the cardiac cycle. At the heart rate of 400–500 per min, there were 8–9 frames per each cycle, and 7–8 cycles were recorded in each x-ray recording, which lasted for $15 \times 70 = 1050$ ms. In this study, only the data with nine frames per cycle were analyzed. The frames that contained the R wave in the electrocardiogram (Fig. 1) were used as the first frame of a cycle (end-diastole). Then, frames in the same phase of the cycle were averaged. Thus, for each recording, a set of images was obtained. As the R wave could take place any time within a frame, the data had an ambiguity of one frame (15 ms) in time. This ambiguity is averaged out because, in total, data from 53 and 58 recordings were used for the baseline and dobutamine conditions, respectively.

Data analysis

Diffraction in the region of the x-ray pattern without contribution from skeletal muscles was circularly averaged. The background was fitted with a cubic spline function, and the area above the background was used as the

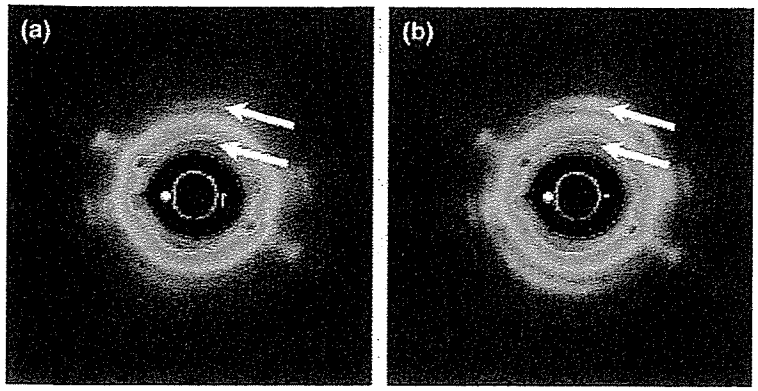

FIGURE 2 X-ray diffraction patterns from a heart in vivo. (*a*) In end-diastole (first frame), (*b*) in systole (fourth frame). The intensity distribution is shown in pseudocolor. The four spots are from skeletal muscles. The rings in the rest of the pattern (*arrows*) are from cardiac muscle: the inner one is the (1,0), and the outer (1,1) equatorial reflection. These are averages of six diffraction patterns from a normal mouse.

diffraction peak (Fig. 4). The integrated area was used as the integrated intensity, and the center of gravity of the (1,0) reflection was converted to the (1,0) lattice spacing. The integrated intensity of the (1,1) reflection obtained this way is underestimated by $\sqrt{3}$ compared to that of the (1,0) reflection because the intensity is averaged, not summed, along an arc. Thus, the (1,1) intensity was multiplied by $\sqrt{3}$. Since the intensity of each equatorial reflection depends on the thickness of the sample, which changes considerably across a heart, the ratio of the intensities of the (1,0) and (1,1) reflections (I(1,0)/I(1,1)) was used as an index of the equatorial intensity change.

Then, data from different x-ray recordings were analyzed. Results from recordings on each mouse were averaged, providing a set of intensity ratios and lattice spacings for each mouse over frames. Then, data sets from 10 mice were treated statistically. The same procedure was used on the data taken after dobutamine infusion.

The half-time of contraction and relaxation was obtained by the following method: 1), The intensity ratio or lattice spacing in the first frame was taken as a diastolic level. 2), The smallest intensity ratio or the largest lattice spacing value was taken as a systolic level. 3), The average of the diastolic and systolic levels was taken as the midlevel. 4), The time when the intensity ratio or lattice spacing crossed the midlevel during the early or late phase of a heart beat was obtained by interpolation between frames and taken as the half-time of contraction or relaxation.

Using the ratio of the (1,0) and (1,1) intensities (I(1,0)/I(1,1)), the electron-density distribution in the transverse section of the hexagonal myofilament lattice was calculated by Fourier synthesis. From this, the mass associated with the thin filaments was estimated following the method of Haselgrove and Huxley (10) on the assumption that the lowest density in the electron-density map represented the background level. The "apparent" thin-filament mass thus calculated was interpreted as consisting of the thin filament and the myosin heads present in the vicinity of the thin filament. The mass of the thin filament was approximated by assuming that no myosin heads are present in the vicinity of the thin filament at the resting state. Then, by subtracting this from the apparent thin-filament mass, the mass of heads associated with the thin filament was obtained. The same procedure was done with the intensity ratio obtained in the rigor state, and the total mass of heads can be obtained by assuming that all heads are attached to the thin filament. From these masses of heads, the proportion of heads present in the vicinity of thin filaments was calculated.

All data are expressed as mean ± SD. Differences were analyzed using Student's paired *t*-test with $p < 0.05$ being regarded as statistically significant.

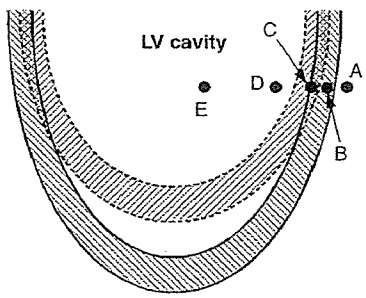

FIGURE 3 Positions of the x-ray beam relative to the left ventricle. The shaded areas represent a left ventricular free wall. The area between solid curves is a wall in diastole, and that between broken curves a wall in systole. At position *A*, the beam is out of the heart. At *B*, the beam is passing through the epicardium in diastole but out of the heart in systole. At *C*, the beam is always in the wall but it is in the epicardium in diastole and in the endocardium in systole. At *D*, the beam is always passing through the wall on both sides of the heart. At *E*, the beam also passes through the wall on both sides but absorption by blood in the cavity hampers the x-ray measurement. In the actual experiment, a mouse (hence a heart) was moved relative to a fixed x-ray beam.

RESULTS

Fig. 2 shows x-ray diffraction patterns from a mouse heart in vivo at end-diastole and systole. Although diffraction spots from skeletal muscles are superposed, arcs of equatorial diffraction from cardiac muscles are clearly seen. The origin of the reflection can be assigned without ambiguity because the skeletal muscle has a smaller filament lattice spacing and hence the reflections appeared at a larger radius. When the region where the equatorial reflections from cardiac muscle were strong, it was possible to subtract background from other tissues such as skin, lung, and skeletal muscle (Fig. 4). Fig. 5 *a* (*open squares*) shows the time course of changes in the (1,0)/(1,1) intensity ratio during a cardiac cycle at baseline. The diastolic intensity ratio was ~2.1 at end-diastole and decreased to a minimum of 0.8 in ~50 ms, which is comparable to the ratios observed in rat heart muscle (13).

Fig. 5 *b* (*open squares*) shows the time course of changes in the (1,0) lattice spacing at baseline. The lattice spacing at end-diastole was 37.2 nm and increased to 39.1 nm within

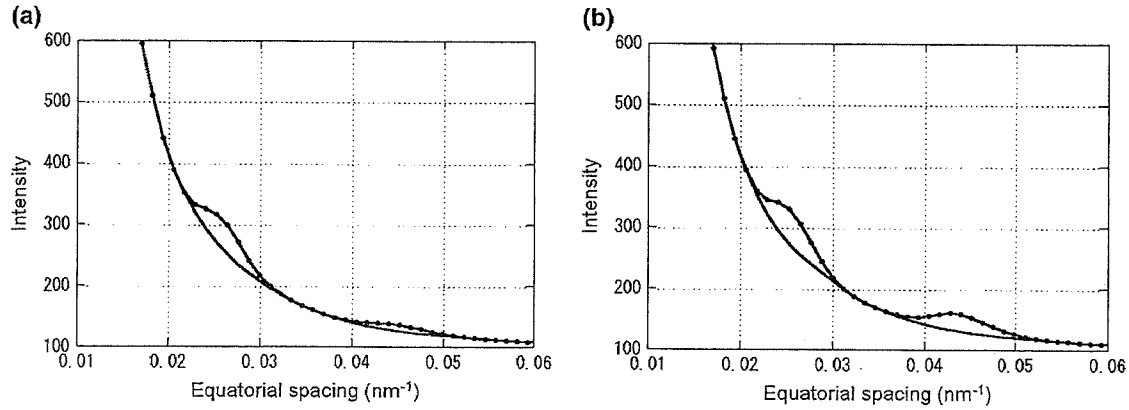

FIGURE 4 Intensity profiles of the (1,0) and (1,1) equatorial peaks. (a) in end-diastole, (*b*) in systole. The data were from Fig. 3, integrated within arcs of 10.5 o'clock through 2 o'clock and its opposite side. The background was drawn using a spline function.

~90 ms after the R wave in the electrocardiogram. If strict constant-volume behavior is assumed, this corresponds to ~10% shortening of sarcomere. The lattice spacing continued to increase after the intensity ratio started to increase (that is, after the muscle began to relax), until the mitral valve opened and the left ventricular volume began to increase.

The experiment was repeated after dobutamine had been infused for 10 min (20 μg/kg/min). The heart rate did not change significantly (from 446 $\pm$ 26 to 449 $\pm$ 26 beats per min, $n = 10$). The systemic blood pressure increased significantly from 83.9 $\pm$ 13.1 to 97.1 $\pm$ 14.9 mmHg ($n = 10$). Fig. 5 *a* (*solid circles*) shows the change in the (1,0)/(1,1) intensity ratio under the influence of dobutamine. The second, third, and fourth data points between 20 and 60 ms after the R wave were significantly lower than those in the control mouse, showing a faster and larger shift of mass of cross-bridges. Fig. 5 *b* (*solid circles*) shows the time course of the (1,0) spacing change. The third and fourth data points are significantly larger than those in the control mouse, showing a faster shortening of muscle. The half-time of the reduction in the intensity ratio was significantly shortened by dobutamine (24.4 $\pm$ 1.4 to 20.3 $\pm$ 1.3 ms, $n = 10$), and that of the lattice spacing was also shortened (52.8 $\pm$ 5.9 to 38.3 $\pm$ 1.8 ms, $n = 10$). The half-relaxation time of the lattice spacing was significantly shorter after dobutamine (112.6 $\pm$ 3.0 to 106.8 $\pm$ 2.8 ms, $n = 10$). Since the larger change in the lattice spacing suggests larger sarcomere shortening, the systolic intensity ratio might be affected by a larger filament overlap in the presence of dobutamine. However, since cardiac muscle normally works at a sarcomere length shorter than 2 μm where the thick and thin filaments are fully overlapped, this effect is not considered significant.

After an experiment, a mouse was killed by overdose of pentobarbital and left for 30 min. Then, a diffraction pattern in the rigor state was recorded. The (1,0)/(1,1) intensity ratio was 0.30 $\pm$ 0.08 ($n = 8$).

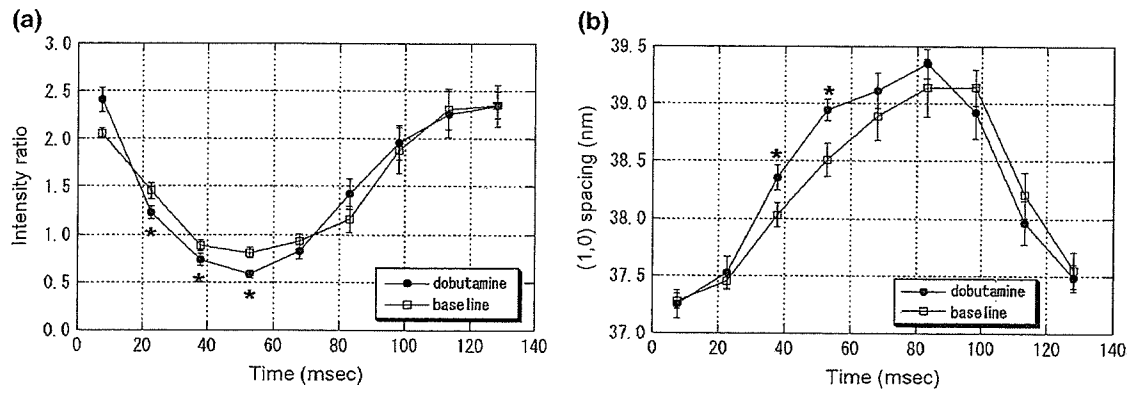

FIGURE 5 Effects of β-stimulation on the cross-bridge activity of mouse heart muscle. (*a*) The (1,0)/(1,1) intensity ratio, (*b*) the (1,0) lattice spacing. The abscissa is the time after the R wave in the electrocardiogram. Open squares represent data obtained before dobutamine infusion, and solid circles after dobutamine infusion (20 μg/kg/ml). The error bars represent the standard error of the mean of data from 10 mice. The asterisks indicate the data points that are statistically different in paired *t*-tests between baseline and dobutamine data.

DISCUSSION

This study is the first, to our knowledge, to investigate myosin cross-bridge activity in a heart in a living body. As stated in the Introduction, it is usually difficult to study murine, especially mouse, cardiac muscle in an isolated specimen under conditions that very closely match physiological. The technique here enables one to investigate mouse cardiac muscle under the most physiological condition, opening a way to study cardiac muscle functions of transgenic mice with x-ray diffraction.

The (1,0) lattice spacing observed in this study (37.2 nm in diastole) is close to that reported in an isolated rat heart with saline perfusion (12), as well as in an isolated intact rat papillary muscle at a sarcomere length of 2.1 μm (7). If we assume that a mouse heart in vivo has the same sarcomere length-lattice spacing relation as an isolated rat papillary muscle, the working range of sarcomere length is between 1.9 and 2.1 μm. On the other hand, a much larger lattice spacing has been reported in a thoractomized rat (13). This may be due to a change in osmolarity which is caused by exposure of the circulatory system to the air. Although the open-chest model of rat has the advantage that pressure and volume of left ventricle can be measured easily during the x-ray measurement, it may be too invasive to study the true physiological state of the heart. The present closed-chest method and the open-chest method should be regarded complementary. A lattice spacing of 34 nm was reported in isolated intact rat trabeculae at a sarcomere length of 2.2 μm (16), which is smaller than the present value. Lattice spacing may be important in cardiac muscle because the distance between myofilaments may affect the contractile tension and play a role in Frank-Starling's law. Previous studies to examine the effect of lattice spacing on tension development were made in skinned fibers which had a (1,0) spacing >40 nm (17,18). It is desirable to investigate the effect at smaller lattice spacings, which are more physiological.

The intensity ratios in diastole and systole found in this study are generally similar to those in previous studies. It has been reported that more cross-bridges are formed in heart muscle preparations that are perfused by blood than in those perfused by saline (9). However, comparison of the results on saline-perfused rat heart (12), on blood-perfused rat heart (13), and from this study on mouse heart under the normal condition shows only small differences. Since the early studies required many contractions to record an x-ray diffraction pattern on a photographic film, deterioration of the sample was probably the major cause of low contractility observed in previous studies on saline-perfused specimens.

In isolated cardiac muscles, it has been found that adrenergic β-stimulation enhances the contractile force and makes both tension development and relaxation faster. This is explained by acceleration of calcium uptake (through phosphorylation of phospholamban) and reduction of the binding affinity of troponin-C to calcium (through phosphorylation of troponin-I) (2–4). These lead to faster development of tension, larger twitch tension, and faster decline of tension in cardiac muscle. In this study, the shorter half-time of reduction in the intensity ratio shows a faster formation of cross-bridges with β-stimulation and the lower minimum intensity ratio shows that more cross-bridges are formed. Although the change in the intensity ratio during relaxation was not clearly accelerated, β-stimulation shortened the half-relaxation time of the lattice spacing. These results demonstrate that the changes of contractile properties previously observed in isolated muscle are actually taking place in a heart muscle in vivo.

In this study, the blood pressure and the amount of myosin cross-bridge formation was increased by dobutamine infusion. On the other hand, the heart rate did not change, indicating that the effects of dobutamine stress were modest. Under this condition, the most interesting finding is that β-adrenergic stimulation does not affect the end-diastolic state. Especially, the lattice spacing at end-diastole was unchanged (Fig. 5 *b*). Since the lattice spacing is related to sarcomere length, this suggests that the left ventricular volume at end-diastole was unaffected. The elevation of blood pressure by β-stimulation was simply due to recruitment of more cross-bridges in cardiac muscle of the free wall. The Frank-Starling mechanism, which would be relevant if the end-diastolic volume were larger and the sarcomere length longer, did not play a major role.

By assuming that all myosin cross-bridges are in the vicinity of the thick filaments in a resting state and that all are bound to the thin filaments in the rigor state, it is possible to calculate the fraction of cross-bridges that are transferred to the vicinity of the thin filaments during contraction (see Methods). In canine cardiac muscle, the resting (quiescent) state may not be the same as the diastolic state (9). However, in rat heart muscle, no such evidence has been found. Thus, the diastolic ratio (the first frame in Fig. 5 *a*) is taken as the resting value. Then, the peak cross-bridge mass transfer ratio under the normal condition is 56%, which increases to 74% by dobutamine infusion. The increase is by 34%, whereas the systemic blood pressure increased by 16%. If we take the resting ratio as an average of those in the absence and presence of dobutamine (2.23), the increase is by 26%. In both cases, the increase in the mass transfer ratio is larger than that in the systemic blood pressure. Since the mass transfer ratio with the β-stimulation (75%) is close to the maximum level observed in tetanus of frog skeletal muscle, the major fraction of cross-bridges is recruited for contraction. Thus, even at this modest level of stress that causes an increase in blood pressure but not in heart rate, most of the potential cross-bridge attachments have been made with few in reserve in the β-stimulated heart.

Weisberg and Winegrad (19) showed by electron microscopy that the heads of the α-isoform of myosin heavy chain are more extended from the backbone of the filament when C-protein was phosphorylated by protein kinase A. Since the

α-isoform is dominant in adult mouse ventricle (20) and β-stimulation causes C-protein phosphorylation (1,3,6), a change in the equatorial intensity ratio is expected. Although the results here do not support this observation, more studies at higher dobutamine stress are needed to clarify the effects of C-protein phosphorylation on the behavior of myosin heads.

The experiments were made with the approval of the SPring-8 Program Review Committee (2002B0142-NL2-np, 2003A0079-NL2-np, 2003B0015-NL3-np, 2004B0319-NL3-np, 2005A0455-NL3-np).

This work was supported by a 2002-2004 Research Grant for Cardiomyopathy (14162201-00) from the Ministry of Health, Welfare, and Labor of Japan and by grants from Uehara Memorial Foundation and the Shimabara Science Promotion Foundation.

REFERENCES

1. Jeacocke, S. A., and P. J. England. 1980. Phosphorylation of a myofibrillar protein of Mr 150 000 in perfused rat heart, and the tentative identification of this as C-protein. *FEBS Lett.* 122:129–132.
2. Kranias, E. G., and R. J. Solaro. 1982. Phosphorylation of troponin I and phospholamban during catecholamine stimulation of rabbit heart. *Nature.* 298:182–184.
3. Garvey, J. L., E. G. Kranias, and R. J. Solaro. 1988. Phosphorylation of C-protein, troponin I and phospholamban in isolated rabbit hearts. *Biochem. J.* 249:709–714.
4. Sulakhe, P. V., and X. T. Vo. 1995. Regulation of phospholamban and troponin-I phosphorylation in the intact rat cardiomyocytes by adrenergic and cholinergic stimuli: roles of cyclic nucleotides, calcium, protein kinases and phosphatases and depolarization. *Mol. Cell. Biochem.* 149–150:103–126.
5. Kentish, J. C., D. T. McCloskey, J. Layland, S. Palmer, J. M. Leiden, A. F. Martin, and R. J. Solaro. 2001. Phosphorylation of troponin I by protein kinase A accelerates relaxation and crossbridge cycle kinetics in mouse ventricular muscle. *Circ. Res.* 88:1059–1065.
6. Hartzell, H. C., and L. Titus. 1982. Effects of cholinergic and adrenergic agonists on phosphorylation of a 165,000-dalton myofibrillar protein in intact cardiac muscle. *J. Biol. Chem.* 257:2111–2120.
7. Yagi, N., H. Okuyama, H. Toyota, J. Araki, J. Shimizu, G. Iribe, K. Nakamura, S. Mohri, K. Tsujioka, H. Suga, and F. Kajiya. 2004. Sarcomere-length dependence of lattice volume and radial mass transfer of myosin cross-bridges in rat papillary muscle. *Pflugers Arch.* 445:238–245.
8. Matsubara, I., N. Yagi, D. W. Maughan, Y. Saeki, and Y. Amemiya. 1989. X-ray diffraction study on heart muscle during contraction. *In* Muscle Energetics. R. J. Paul, G. Elzinga, and K. Yamada, editors. Alan T. Liss, New York. 481–486.
9. Matsubara, I. 1980. X-ray diffraction studies on the heart. *Annu. Rev. Biophys. Bioeng.* 9:81–105.
10. Haselgrove, J. C., and H. E. Huxley. 1973. X-ray evidence for radial cross-bridge movement and for the sliding filament model in actively contracting skeletal muscle. *J. Mol. Biol.* 77:549–568.
11. Huxley, H. E., R. M. Simmons, A. R. Faruqi, M. Kress, J. Bordas, and M. H. J. Koch. 1983. Changes in the x-ray reflections from contracting muscle during rapid mechanical transients and their structural implications. *J. Mol. Biol.* 169:469–506.
12. Yagi, N., J. Shimizu, S. Mohri, J. Araki, H. Nakajima, Y. Okumura, H. Toyota, T. Morimoto, Y. Morizane, M. Kurusu, T. Miura, K. Hashimoto, K. Tsujioka, H. Suga, and F. Kajiya. 2004. X-ray diffraction from a left ventricular wall of rat heart. *Biophys. J.* 86:2286–2294.
13. Pearson, J. T., M. Shirai, H. Ito, N. Tokunaga, H. Tsuchimochi, N. Nishiura, D. O. Schwenke, H. Ishibashi-Ueda, R. Akiyama, H. Mori, H. Kangawa, H. Suga, and N. Yagi. 2004. In situ measurements of crossbridge dynamics and lattice spacing in rat hearts by x-ray diffraction: sensitivity to regional ischemia. *Circulation.* 109:2983–2986.
14. Inoue, K., T. Oka, T. Suzuki, N. Yagi, K. Takeshita, S. Goto, and T. Ishikawa. 2001. Present status of high flux beamline (BL40XU) at SPring-8. *Nucl. Instrum. Meth. A.* 467–468:674–677.
15. Amemiya, Y., K. Ito, N. Yagi, Y. Asano, K. Wakabayashi, T. Ueki, and T. Endo. 1995. Large-aperture TV detector with a beryllium-windowed image intensifier for x-ray diffraction. *Rev. Sci. Instrum.* 66:2290–2294.
16. Irving, T. C., J. Konhilas, D. Perry, R. F. Fischetti, and P. P. de Tombe. 2000. Myofilament lattice spacing as a function of sarcomere length in isolated rat myocardium. *Am. J. Physiol.* 279:H2568–H2573.
17. Konhilas, J. P., T. C. Irving, and P. P. de Tombe. 2002. Myofilament calcium sensitivity in skinned rat cardiac trabeculae: role of interfilament spacing. *Circ. Res.* 90:59–65.
18. Wang, Y. P., and F. Fuchs. 1995. Osmotic compression of skinned cardiac and skeletal muscle bundles: effects on force generation, Ca^{2+} sensitivity and Ca^{2+} binding. *J. Mol. Cell. Cardiol.* 27:1235–1244.
19. Weisberg, A., and S. Winegrad. 1998. Relation between crossbridge structure and actomyosin ATPase activity in rat heart. *Circ. Res.* 83:60–72.
20. Lyons, G. E., S. Schiaffino, D. Sassoon, P. Barton, and M. Buckingham. 1990. Developmental regulation of myosin gene expression in mouse cardiac muscle. *J. Cell Biol.* 111:2427–2436.

Increased eNOS Accounts for Changes in Connexin Expression in Renal Arterioles During Diabetes

JIAN HONG ZHANG,[1] SEINOSUKE KAWASHIMA,[2] MITSUHIRO YOKOYAMA,[2] PAUL HUANG,[3] AND CARYL E. HILL[1]*

[1]Division of Neuroscience, John Curtin School of Medical Research, Australian National University, Canberra, Australia
[2]First Department of Internal Medicine, Kobe University School of Medicine, Kobe, Japan
[3]Harvard Medical School, Cardiovascular Research Centre, Massachusetts General Hospital, Charlestown, Massachusetts

ABSTRACT

Previous studies have shown that connexin (Cx) expression is considerably higher in the preglomerular compared to postglomerular vasculature and that these differences are accentuated during diabetes. Since nitric oxide (NO) has been reported to alter Cx expression in endothelial cells and muscle cells and NO bioavailability is altered in diabetes, we hypothesized that NO may be responsible for the changes during diabetes. Cx expression was studied using immunohistochemistry in mice in which eNOS expression was either upregulated (eNOS transgenic) or downregulated (eNOS knockout). Diabetes was induced intraperitoneally with a single dose of alloxan or multiple low doses of streptozotocin. Expression of Cx40 in smooth muscle cells of afferent arterioles was increased, while expression of Cx43 in endothelial cells of efferent arterioles was absent in eNOS transgenic mice, similar to the changes occurring in wild-type mice during diabetes. Expression of Cx40 and Cx43 in eNOS knockout mice was not different from control; however, induction of diabetes in eNOS knockout mice failed to produce any changes in Cx40 or Cx43 in either afferent or efferent arterioles. Immunohistochemistry showed that eNOS expression was increased in the endothelium of renal arterioles in wild-type diabetic and eNOS transgenic mice, but absent from arterioles of eNOS knockout mice. We conclude that changes occurring in Cx expression in afferent and efferent arterioles during diabetes may result from increased eNOS. Anat Rec Part A, 288A:1000–1008, 2006.

Key words: eNOS; connexin; renal arterioles; diabetes

Regulation of regional blood flow and the maintenance of systemic blood pressure require integration and coordination of vascular responses within different vascular beds. The ability of arterioles to conduct vasoconstriction and vasodilation over distance along the vascular tree is critical to the local modulation of vascular resistance (Christ et al., 1996; Hill et al., 2002; Segal, 2005). This complex intrinsic integration and coordination process depends on gap junctions, which are intercellular communication channels composed of connexin molecules (Cx) (Hill et al., 2001). In studies of many different arteries

Grant sponsor: The National Heart Foundation; Grant number: Grant-in-Aid G03C 1059.

*Correspondence to: Caryl E. Hill, Division of Neuroscience, John Curtin School of Medical Research, Australian National University, Canberra, ACT 2602, Australia. Fax: 61-2-6125-8077. E-mail: caryl.hill@anu.edu.au

Received 14 May 2006; Accepted 9 June 2006
DOI 10.1002/ar.a.20369
Published online 4 August 2006 in Wiley InterScience (www.interscience.wiley.com).

and arterioles, Cxs37, 40, and 43 have been readily detected between adjacent endothelial cells, while Cx expression is more limited among smooth muscle cells, particularly in resistance arteries and arterioles and the specific subtype debatable (Hill et al., 2001, 2002).

A number of factors have been described to modulate Cx expression, conductance, and permeability of gap junctions to cytosolic molecules (Harris, 2001). In vitro studies have shown that exogenous nitric oxide (NO) increased the expression of Cx40 in endothelial gap junctions (Hoffmann et al., 2003) and Cx43 expression in mesangial cells (Yao et al., 2005) but decreased Cx43 expression in uterine myocytes (Sladek et al., 1999; Roh et al., 2002). Elevated glucose has also been shown to inhibit gap junctional communication in cultured smooth muscle cells through alterations to the phosphorylation of Cx43 (Kuroki et al., 1998) and in cultured microvascular endothelial cells through downregulation of Cx43 expression (Sato et al., 2002).

In our previous experiments, we demonstrated extensive expression of Cxs37, 40, and 43 in endothelial cells and Cx37 in smooth muscle cells of the preglomerular renal vasculature but only Cx43 in endothelial cells of the postglomerular vasculature (Zhang and Hill, 2005). Cxs37 and 40 were expressed strongly in the renin-secreting cells. During diabetes, expression of Cx40 was increased in smooth muscle cells of the afferent arterioles while Cx43 was decreased in endothelial cells of the efferent arterioles (Zhang and Hill, 2005). Since previous studies have shown that the bioavailability of NO is altered during diabetes (Prabhakar, 2004; Schalkwijk and Stehouwer, 2005), the aim of the present study was to determine whether changes in endothelial NO were responsible for the changes in Cx expression observed in the juxtaglomerular apparatus. For these studies, we used genetically modified mice in which endothelial nitric oxide synthase (eNOS) expression was either upregulated (eNOS transgenic) or downregulated (eNOS knockout). To test the involvement of eNOS in Cx changes during diabetes, we induced diabetes in eNOS gene-modified mice using streptozotocin or alloxan.

MATERIALS AND METHODS

Experiments were performed under a protocol approved by the Animal Experimentation Ethics Committee of the Australian National University. All procedures were conducted in accordance with the Australian Code of Practice for the Care and Use of Animals for Scientific Purposes. Mice were housed under 12-hr light/dark cycles and given food and water ad libitum.

Animals

In eNOS transgenic mice, overexpression of the bovine eNOS gene in endothelial cells of the vascular wall (Ohashi et al., 1998) was achieved through the use of the murine preproendothelin-1 promoter (Harats et al., 1995). Characterization of this mouse has been published previously (Ohashi et al., 1998; Yamashita et al., 2000; Kawashima et al., 2001; Ozaki et al., 2002); eNOS transgenic mice were hypotensive (Ohashi et al., 1998). eNOS knockout mice were created by targeted disruption of the eNOS gene and confirmed by Southern and Western blot analysis. These mice developed hypertension (Huang et al., 1995).

Heterozygous eNOS transgenic mice were backcrossed to wild-type C57BL/6 for at least seven generations while eNOS knockout mice were inbred. Age- and sex-matched wild-type C57BL/6 mice were used as control (Huang et al., 1995), in addition to the negative littermates of transgenic matings, as preliminary experiments did not demonstrate any differences between these groups. Identification of eNOS transgenic founder mice and offspring was done by PCR genotyping. Primers were 5′-GGTCTTATCTCTGGCTGCACGTT-3′ (sense, located in the preproendothelin-1 promoter) and 5′-CACAGAGTGTCGTAGGTGATGCT-3′ (antisense, located in the eNOS gene), giving a product of 582 bp. PCR conditions were 95°C for 15 sec, 65°C for 15 sec, 72°C for 60 sec; 35 cycles. The published eNOS transgenic sequence (Ohashi et al., 1998) was confirmed by DNA cloning and sequencing of the PCR product.

Diabetes Protocol

Diabetes was induced in male eNOS transgenic mice, their negative littermates, and eNOS knockout mice (8–10 weeks) by intraperitoneal injection of either a single-dose alloxan (5,6-dioxyuracil monohydrate; 175 mg/kg body weight; Sigma-Aldrich, St. Louis, MO) in normal saline or multiple low doses of streptozotocin [2-deoxy(3-methyl-3-nitrosoureido)-D-glucopyranose; 40 mg/kg body weight; Calbiochem, Darmstadt, Germany] in 0.2 M acetate-buffered saline (pH 4.4) on 5 consecutive days. The former method produces a rapid rise in blood glucose and drug-induced death of pancreatic β-cells (Szkudelski, 2001), while the latter approximates more closely human diabetes with a slower death of β-cells due to insulitis (Paik et al., 1980). Both methods were used to induce diabetes in all three groups of mice.

Capillary blood glucose level was determined using Medisense blood glucose electrode sensor (Abbott Laboratories, Victoria, Australia). Diabetes was defined as a nonfasting capillary blood glucose level $\geq$ 15 mM. Vehicle-injected mice were used as control. Blood glucose levels and body weight were monitored twice a week. Intraperitoneal supplement of saline was given to mice whose body weight loss was more than 1 g/day. This only applied to the mice treated with a single dose of alloxan and occurred in the first and occasionally in the second week following injection.

Our preliminary studies showed that the changes in Cx expression in diabetes induced with a single-dose alloxan in wild-type C57BL/6 mice were maximal after 8 to 10 weeks of established diabetes, as we had previously found for high doses of streptozotocin (Zhang and Hill, 2005). Our preliminary data with mice in which diabetes was induced with multiple low doses of streptozotocin showed that similar Cx changes occurred but these were not maximal until 14 to 16 weeks of established diabetes. These times formed the endpoints for our studies. It should be noted, however, that the duration of diabetes was similar for the two methods since diabetes was induced rapidly in the case of alloxan, i.e., by day 3 postinjection, but slowly in the case of multiple low doses of streptozotocin, i.e., 30 to 40 days postinjection. Consequently, the duration of diabetes for both methods was 8–10 weeks.

Immunohistochemistry

Male wild-type, eNOS transgenic, and eNOS knockout mice and their diabetic counterparts (n = 4, minimum for each group) were deeply anesthetized (5 mg/kg xylazine and 25 mg/kg ketamine, i.p.). Fresh renal blocks were fixed in acetone (4°C for 30 min), thoroughly washed with phosphate-buffered saline (PBS), immersed in 30% sucrose in PBS (4°C overnight), and embedded in Cryo-M-Bed (Bright Instrument, Cambridge, U.K.). Coronal sections were cut at 30 μm, mounted onto 2% silane (Sigma-Aldrich, Sydney, Australia)-coated slides, dried, and stored frozen.

Frozen tissue sections were preincubated in 2% BSA and 0.2% Triton in PBS and then in sheep antibodies against rat Cxs37, 40 (1:250) (Rummery et al., 2002), or rabbit antibody against rat Cx43 (1:250; Zymed Laboratories, San Francisco, CA) in the same solution for 48 hr at room temperature. The specificity of these three antibodies has been confirmed previously by Western blotting and immunohistochemistry of COS-7 cells transfected with plasmid DNA encoding either Cxs37, 40, or 43 (Rummery et al., 2005). Specific Cx subtype staining was detected using either Cy3-conjugated antigoat IgG (1:600; Jackson ImmunoResearch Laboratories, West Grove, PA) or Alexa Fluor 568-conjugated antirabbit IgG (1:600; Molecular Probes, Eugene, OR) in 0.2% Triton in PBS for 2 hr.

For assessment of eNOS protein expression, fresh renal blocks were immersion-fixed in 2% paraformaldehyde in 0.1 M sodium phosphate buffer (pH 7.4) for 10 min at room temperature. For assessment of iNOS protein expression, renal blocks were fixed in cold acetone for 30 min. In both cases, tissue blocks were further processed as indicated above.

Expression of eNOS and iNOS protein was determined with rabbit polyclonal anti-eNOS (1:100; Abcam, Cambridge, U.K.) and anti-iNOS (1:1,000; Zymed Laboratories, South San Francisco, CA), subsequently detected with Alexa Fluor 568-conjugated antirabbit IgG (1:600). The specificity of eNOS and iNOS antibodies was tested on renal tissues from eNOS knockout and iNOS knockout mice, respectively. Identification of vascular smooth muscle cells was achieved by subsequent labeling with rabbit antimyosin (U. Gröschel-Stewart, Technische Universitat, Darmstadt, Germany; 1:250) detected by FITC-conjugated antirabbit IgG (Dako, Denmark, 1:40).

Collection and Analysis of Data

Images were obtained using a confocal laser scanning microscope and Argon/Kryton laser (TCS 4D; Leica Instruments, Vienna, Austria). Serial images at 1 μm intervals were obtained in the Z-axis, encompassing entire blood vessels and recombined. For dual-labeled sections, either composite or individual images were combined in Adobe Photoshop as indicated. For comparisons using the same antibody in tissues from different animals, images were obtained at the same pinhole, laser intensity, and voltage settings. For each animal, at least four pictures from four different visual fields were taken and for each group four different animals were included. In order to assess the extent of nonspecific staining, the primary antibody was preincubated with the appropriate antigenic peptide before being applied to tissue sections or the primary antibody was omitted. Alternatively, solutions containing the primary antibody were applied to tissue sections from the relevant gene knockout mice, for example, anti-eNOS applied to tissues from eNOS knockout mice.

Semiquantification of Cx staining was undertaken on confocal images of afferent arterioles (Cxs37, 40) and efferent arterioles (Cx43). Assessment of the amount of staining among the control and diabetic mice groups was made blindly by two people (one of the two authors and another independent person) using unlabeled micrographs representing afferent or efferent arterioles from a minimum of four different animals in each group. This method allowed differentiation of Cx staining between smooth muscle cells and endothelial cells in afferent arterioles, which was not possible using the computer-based software program in our previous studies (Zhang and Hill, 2005).

The level of Cx37 expression in smooth muscle cells of afferent arterioles was assessed from + to +++, representing, respectively, no Cx staining beyond renin-secreting cells; weak and irregular Cx staining; strong, uniform Cx staining.

Cx43 expression in endothelial cells of efferent arterioles was categorized from + to +++, representing, respectively, no Cx staining; Cx staining in efferent arterioles but less than in afferent arterioles; Cx staining in efferent arterioles equivalent to that in afferent arterioles.

Cx40 expression in smooth muscle cells of afferent arterioles was categorized from + to ++++, representing, respectively, no Cx staining beyond renin-secreting cells; staining in muscle cells immediately adjacent to renin-secreting cells (usually within 40 μm); weak staining in muscle cells located beyond 40 μm from renin-secreting cells; strong staining in distal smooth muscle cells.

For statistical analysis, the semiquantitative variables (+ to ++++) were assigned a value from 1.0 to 4.0. Data were expressed as mean ± SEM and analyzed using one-way ANOVA and nonpaired *t*-test with Bonferroni correction for multiple comparisons. Statistical significance was set at $P < 0.05$.

RESULTS

All the diabetic mice injected with multiple low doses of streptozotocin survived to the endpoint of the experiments and the body weight of diabetic mice was not significantly different to that of control mice (wild-type control, 26.9 ± 1.08 g; wild-type diabetic, 24.6 ± 0.65 g; eNOS transgenic control, 24.7 ± 0.84 g; transgenic diabetic, 24.2 ± 0.65 g; eNOS knockout control, 27.2 ± 2.19 g; knockout diabetic, 26.1 ± 1.54 g). In the case of diabetes induction with a single dose of alloxan, 20% of the wild-type and eNOS knockout mice and all of the eNOS transgenic mice died before the endpoint of the experiment. Body weights of surviving diabetic mice were not significantly different to those of control mice (wild-type control, 25.3 ± 0.83 g; wild-type diabetic, 23.9 ± 0.16 g; eNOS transgenic control, 24.7 ± 0.87 g; eNOS knockout control, 26.2 ± 0.76 g; knockout diabetic, 23.0 ± 1.96 g).

Renal arterioles were identified with antimyosin staining. Afferent arterioles were distinguished from efferent arterioles by their larger diameter in the superficial cortex, absence of branching prior to entering the glomerulus, direct communication with larger interlobular